공학박사 학위논문

Myelin Water Imaging
for Clinical Research

임상연구를 위한 신경수초물영상

2019 년 2 월

서울대학교 대학원

전기 · 정보공학부

최 준 열

Myelin Water Imaging
for Clinical Research

지도 교수 이 종 호

이 논문을 공학박사 학위논문으로 제출함
2019 년 2 월

서울대학교 대학원
전기 · 정보공학부
최 준 열

최준열의 공학박사 학위논문을 인준함
2019 년 2 월

위 원 장 _____최 승 홍_____ (인)

부위원장 _____이 종 호_____ (인)

위　　원 _____김 호 진_____ (인)

위　　원 _____김 정 훈_____ (인)

위　　원 _____오 세 홍_____ (인)

초   록

신경수초는 몸 안의 전기적 신호를 전달하는데 있어 중요한 역할을 한다. 신경퇴행성질환은 신경수초 손상과 연관성이 있으며 이는 전기적 신호 전달의 손실을 유발한다. 병원에서 사용하는 자기 공명 영상법인 T_1, T_2 강조영상들은 신경수초의 양을 정량화 할 수 없고 신경퇴행성질환 환자의 신경수초의 손상된 정도를 확인 할 수 없다. 본 연구에서는 신경수초의 손상된 정도를 예측하기 위해 새롭게 개발 된 신경수초물영상을 신경퇴행성질환에 적용하였다. 이를 위해 신경다발의 물교환 및 머리로 유입되는 혈류로 인한 신경수초물영상법에 미치는 영향에 대하여 탐구하였다. 또한, 신경수초물영상법을 이용한 임상적 연구를 위하여 분석 파이프라인을 개발하였다. 첫째로 신경다발의 생물, 물리적학적 특성을 시뮬레이션화한 Monte-Carlo 시뮬레이션 모델을 개발하였다. 시뮬레이션에서 계산된 신경수초물의 거주 시간을 이용하여 신경수초물영상법이 신경수초물을 측정하고 있는 것을 검증하였다. 둘째로 본 연구에서는 머리로 유입되는 혈류로 인한 artifact을 제거하기 위해 혈류 시뮬레이션 모델을 개발하였다. 혈류 시뮬레이션 모델을 통하여 유입되는 혈류로 인한 artifact을 최소화 하는 혈류포화펄스의 최적 시간을 제안하였다. 최종적으로, 신경수초물 영상의 임상연구 적용을 위하여 분석 파이프 라인을 개발 및 요약하였다. 이를 이용하여 신경퇴행성질환인 다발성경화증, 시신경척수염, 외상성 뇌손상 환자의 정상으로 보이는 영역에서 신경수초물변화를 관찰하였다. 본 연구의 결과는 추후 수초관련 뇌 질환의 진단, 치료의 효용성 및 예후 평가뿐 아니라 학습에 의한 뇌 가소성 연구 및 재활 치료 효과 평가에 이용될 수 있을 것이라 사료된다.

주요어 : 자기공명영상, 수초, 두뇌, 백색질, 수초물영상, 미세구조영상
학   번 : 2015-30205

Contents

List of Tables

List of Figures

List of Abbreviations

Abbreviation	Term
aMWF	Apparent myelin water fraction
CS	Centrum semiovale
DTI	Diffusion tensor imaging
EPI	Echo-planar imaging
FA	Fractional anisotropy
FS	Visual function system
GN	Genu of corpus callosum
GRASE	Gradient echo and spin echo
GRE	Gradient echo
MTI	Magnetization transfer imaging
MWF	Myelin water fraction
MWI	Myelin water imaging
MS	Multiple sclerosis
NAWM	Normal-appearing white matter
NMOSD	Neuromyelitis optica spectrum disorder
NWM	Normal white matter
OR	Optic radiation
PD GRE	Proton density weighted gradient echo
PVWM	Periventricular white matter

RD	Radial diffusivity
ROI	Region of interest
SPL	Splenium of corpus callosum
TBI	Traumatic brain injury
TD	Duration between excitation pulse and first inversion
TE	Echo time
TI_1	Duration between first inversion and second inversion
TI_2	Duration between second inversion and excitation pulse
TR	Repetition time
T_1	Longitudinal relaxation
T_2	Transverse relaxation
WM	White matter
ViSTa	Direct visualation of short transverse relaxation time component

Note

Some parts of the thesis are extracted from the journal publications. The publications were published during the course of the study.

Jeong IH[+], Choi JY[+], Kim SH, et al. Comparison of myelin water fraction values in periventricular white matter lesions between multiple sclerosis and neuromyelitis optica spectrum disorder. *Multiple sclerosis*. 2016;22(12):1616-1620.

Jeong IH[+], Choi JY[+], Kim SH, et al. Normal appearing white matter demyelination in neuromyelitis optica spectrum disorder. *European Journal of Neurology*. 2017;24(4):652-658.

Choi JY, Jeong IH, Oh SH, et al. Evaluation of Normal-Appearing White Matter in Multiple Sclerosis Using Direct Visualization of Short Transverse Relaxation Time Component (ViSTa) Myelin Water Imaging and Gradient Echo and Spin Echo (GRASE) Myelin Water Imaging. *Journal of magnetic resonance imaging*. 2018 DOI:10.1002/jmri.26278.

Chapter 1. Introduction

1.1 Myelin

Myelin is a fatty substance covering axon. Oligodendrocytes form myelin in the central nervous system and Schwann cells form myelin in the peripheral nervous system. Myelin increases the speed of neural signals by saltatory conduction. The saltatory conduction of neural signal occurs in the node of Ranvier. Hence, the speed of myelin-rich axons is faster than the speed of myelin-less axons. If myelin is damaged, nerves do not conduct electrical impulses normally. Therefore, measurement of myelin is important in neurological disorders such as multiple sclerosis (MS), neuromyelitis optica spectrum disorder (NMOSD), traumatic brain injury (TBI), Alzheimer's disease and etc.

1.2 Myelin Water

Myelin water is water molecules trapped between lipid bilayers in myelin sheath as shown in Figure 1. In MRI, many studies have investigated the characteristics of myelin water (1-5). Table 1 summarizes the characteristics of myelin water.
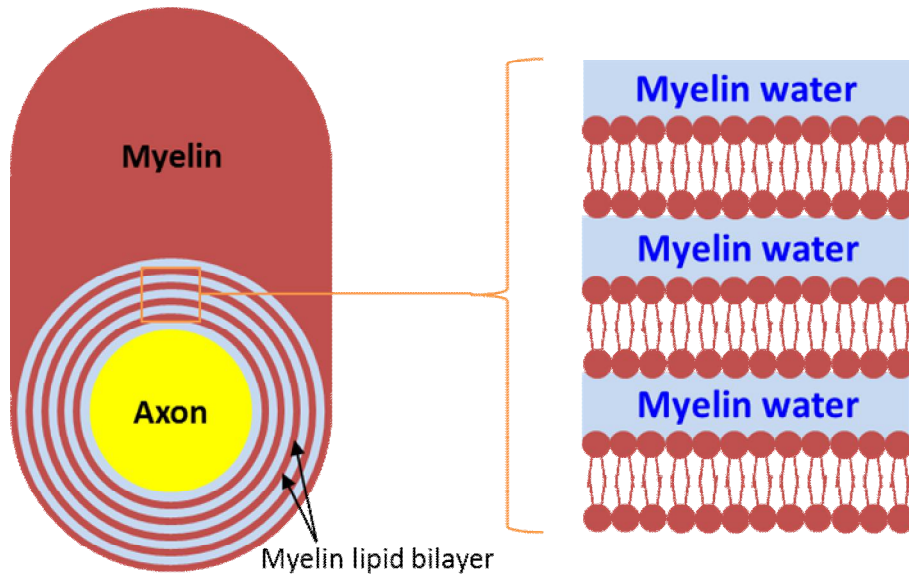
Figure 1. Myelinated axon and myelin water between lipid bilayers in myelin sheath. Myelin water is trapped between myelin lipid bilayers.

Myelin water has shown to have short T_2 (less than 40 ms), T_2^* (Less than 15 ms), and shorter apparent T_1 than other water T_1 (2,3,5,6). Additionally, myelin water has been demonstrated to have the opposite frequency shift to axonal water when the fiber is perpendicular to the external magnetic field (1). Due to large interactions between myelin water and lipid bilayers, myelin water has about 40% magnetization transfer effects (4).

Table 1. Characteristics of myelin water

Characteristics	Myelin water
T_2	Less than 40 ms (5)
T_2^*	Less than 15 ms (3)
T_1	Shorter than other water (2)
Frequency shift (perpendicular fiber)	Opposite to axonal water (positive) (1)
Magnetization transfer ratio	40% (4)

Because of the T_2 difference between myelin water and axonal/extra-cellular water, a signal decay curve from T_2 decay in white matter shows a multi-exponential decay curve (Figure 2). T_2 of axonal water and extra-cellular water is approximately 80 to 100 ms whereas myelin water is less than 40 ms (5). Using this T_2 property, myelin water can be separated from the entire signal using the non-negative least square fitting of multi-exponential functions (Figure 2). This approach is conventional myelin water imaging (MWI). Then, myelin water fraction (MWF) is calculated by dividing a myelin water signal by the total water signal (Figure 2). However, the image quality of conventional MWI is low since the multi-exponential fitting is an ill-conditioned problem.
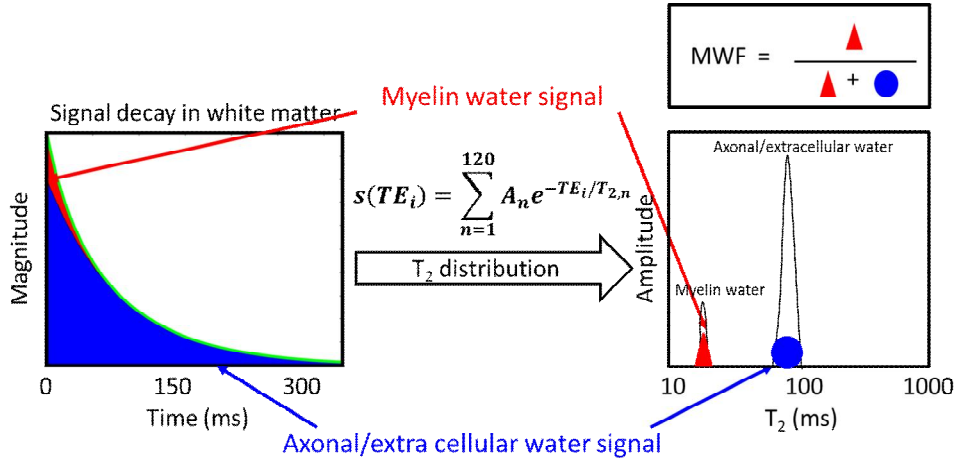
Figure 2. Multi-exponential curve of white matter signal (left) and T_2 distribution of white matter signal (right). T_2 distribution is calculated by non-negative least square algorithm. Myelin water fraction is a ratio of myelin water signal to total water signal.

1.3 ViSTa Myelin Water Imaging

1.3.1 ViSTa Sequence

Direct visualization of short transverse relaxation time component (ViSTa) is a new approach that selectively acquires short T_2^* to measure myelin water signal (7). The schematic diagram of ViSTa sequence is shown in Figure 3.
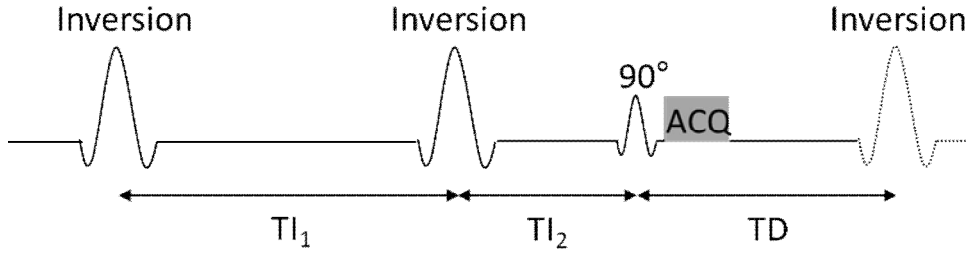
Figure 3. Schematic diagram of ViSTa sequence (7). TI_1 is the duration between first inversion and second inversion. TI_2 is the duration between second inversion and excitation pulse. TD is the duration between excitation pulse and first inversion.

The ViSTa sequence utilizes double inversion preparation pulses to suppress long T_1 signals from axonal and extra-cellular water. Therefore, the ViSTa signal is from myelin water that has short apparent T_1 due to cross relaxation (Figure 4).

The equation of ViSTa signal is as follows.

$$M_{xy} = M_0 \left(1 - \left(2 - (2 - e^{-TD/T_1}) e^{-TI_1/T_1} \right) e^{-TI_2/T_1} \right) e^{-TE/T_2^*}$$

where the three intervals (TI_1, $T1_2$, and TD) are the time between the RF pulses in Figure 3.

5
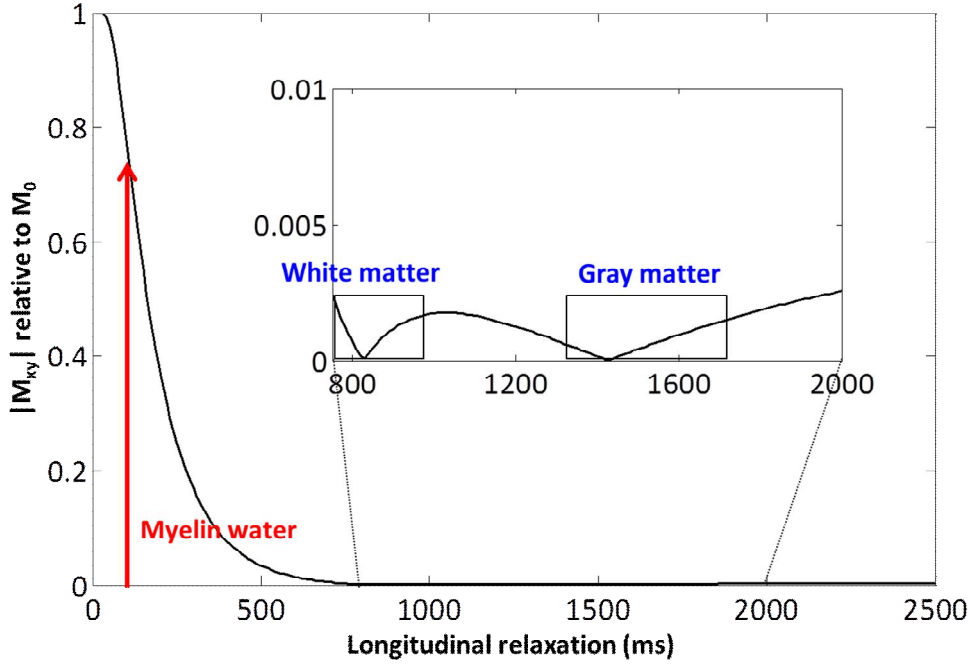
Figure 4. Transverse magnetization as a function of T_1 in ViSTa sequence (7)

1.3.2 Characteristics of ViSTa Signal

A few in-vivo studies have confirmed that the ViSTa signal has the characteristics of myelin water. T_2^* of ViSTa is demonstrated to have less than 15 ms, which is in the range of myelin water (7). The frequency shift of the ViSTa signal is shown to be the opposite to that of gradient echo (GRE) signal when the fiber is perpendicular to the external magnetic field (ViSTa = positive and GRE = negative) (8). The ViSTa signal has shown to have high magnetization transfer ratio (52 ± 15%), agreeing with that of myelin water (9). The characteristics of ViSTa signal are summarized in Table 2. Additionally, the ViSTa signal has shown high correlation with conventional MWI (r = 0.81) (10).

Table 2. Characteristics of ViSTa and GRE signals

Characteristics	ViSTa signal	GRE signal
T_2^* (7)	Less than 15 ms	Between 50 and 100 ms
Frequency shift (perpendicular fiber) (8)	Positive	Negative
Magnetization transfer ratio (9)	$52 \pm 14\%$	$7.3 \pm 5\%$

1.4 Purpose of Study

The primary purpose of the study is to apply ViSTa MWI to neurodegenerative diseases. To utilize ViSTa MWI in clinical studies, I explored the effects of water exchange and inflow in ViSTa MWI. Then, I developed new data analysis pipelines to apply ViSTa MWI for the clinical studies. The subsequent three chapters are as follows: The second chapter is to understand the effects of water exchange in ViSTa by developing Monte-Carlo computer simulation. The third chapter describes a blood flow simulation model to decide the optimal timing of flow saturation pulses for ViSTa MWI. The fourth chapter summarizes new data analysis pipelines for ViSTa MWI. Using the analysis pipelines, ViSTa MWI is applied to investigate the white matter characteristics of three prominent brain diseases and injury, multiple sclerosis (11), neuromyelitis optica spectrum disorder (12,13), and traumatic brain injury.

Chapter 2. Water Exchange Model

2.1 Introduction

As described in Chapter 1, ViSTa MWI has been proposed to acquire short T_2^* signals ($T_{2\_S}^*$) by suppressing long T_1 (T_{1-L}) signals using double inversion preparation pulses (7). However, there is no study that explored the effects of water exchange between myelin water compartment and axonal/extra-cellular compartment. In this chapter, I propose a Monte-Carlo simulation model that mimics water motions in white matter to investigate the ViSTa signal depending on water exchange.

2.2 Methods

2.2.1 Structure

A white matter fiber model applied in this study consisted of three compartments including axonal space, myelin sheath, and extra-cellular space. In the simulation, T_{2-S}^*, T_1 (T_{1-S}) for myelin water were assigned to be 10 ms and 100 ms, respectively while T_2^* (T_{2-L}^*) and T_{1-L} for axonal and extra-cellular water were 50 ms and 800 ms, respectively. A relative proton density of myelin sheath was set to be 70% compared to axonal and extra-cellular spaces. In addition to the relaxation properties, g-ratio (=axon radius/fiber radius) and fiber volume fraction

8

were assumed to be 0.77 and 0.5, respectively (1) while myelin thickness was 133.36 nm. Water molecule size was 0.1 nm.

2.2.2 Monte-Carlo Simulation

Water molecules moved randomly in space and their phases were accumulated according to the location of the water molecules. For simplification, the study considered the movement of water molecules in two dimensions. In each direction, the displacements of the water molecules followed a Gaussian distribution with zero mean and unit standard deviation

$$X = \sqrt{2D \times \Delta t} \text{ and } Y = \sqrt{2D \times \Delta t}$$

where X and Y indicate the directions of the water molecules, D is diffusion coefficient of 1 μm^2/ms, and Δt is a simulation unit step of 10^{-7} s. We used 10,000 water molecules to generate the results once. In each step, both the position and the mean phase of the water molecules were updated and the sum of transverse magnetization (M_{xy}) of three compartments was calculated by following Bloch equation.

$$M_{xy} = M_0 \cdot exp(-i\omega\Delta t) \cdot \{exp(-\Delta t/T^*_{2-S}) + exp(-\Delta t/T^*_{2-L}) + exp(-\Delta t/T^*_{2-L})$$

where M_0 is accumulated M_{xy} and ω is frequency offset due to the magnetic

susceptibility according to the position The frequency offset of this stimulation is shown in Figure 5 (1).
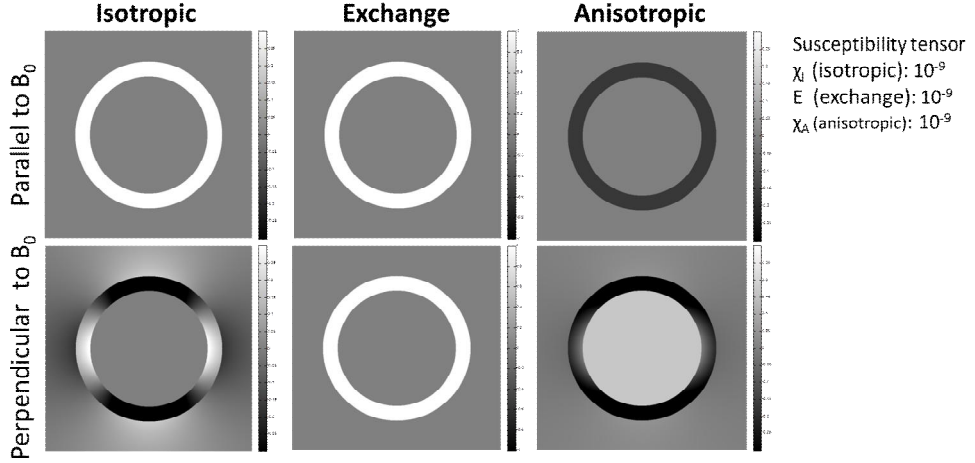
Figure 5. Frequency offsets in simulation (1).

Permeability was defined by pass probability between compartments. The position of water molecules was defined as the distance from the center to the water molecules in two dimensions. The simulation was designed to have water molecules moving to other compartments when it reached the boundary between compartments when satisfied the pass probability. We investigated the various pass probabilities from 100 to 0%. Water molecules distributed randomly in proportion to the size of each compartment for the seeding points.

To demonstrate the effect of ω term on the signal, a simulation was performed to investigate the signal changes with and without a linear gradient field in static dephasing regime (Figure 6). The result shows that the signal with the linear gradient field decayed faster than that without it, confirming the effect of ω term on
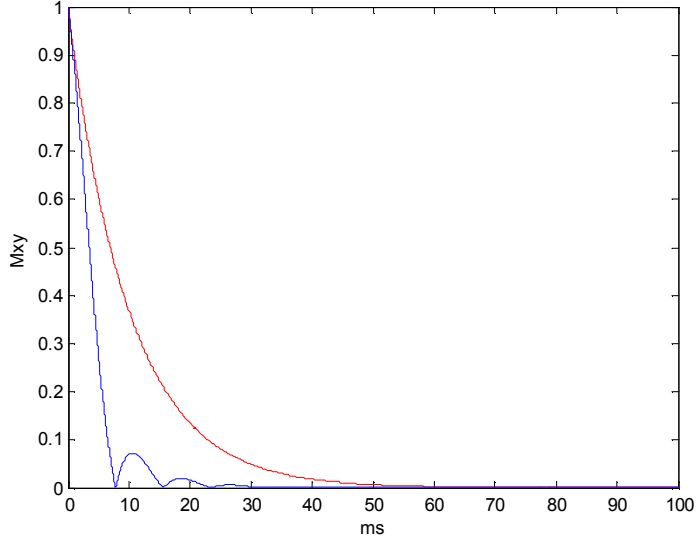
the signal.

Figure 6. Signal decay with (blue) and without (red) a linear gradient field in

static dephasing regime

To validate the effect of the random walk of the simulation on the signal, this study additionally investigated the signal changes with and without water motions (i.e. motional narrowing effect). For the validation, the pass probability was set to be 100%. When there was normal diffusion, the speed of signal decay with a linear gradient field became similar to that without it, confirming the effects of the random walk of the simulation on the signal (Figure 7). Additionally, when there was slow diffusion, the motional narrowing effect became smaller than that of the normal diffusion.

11
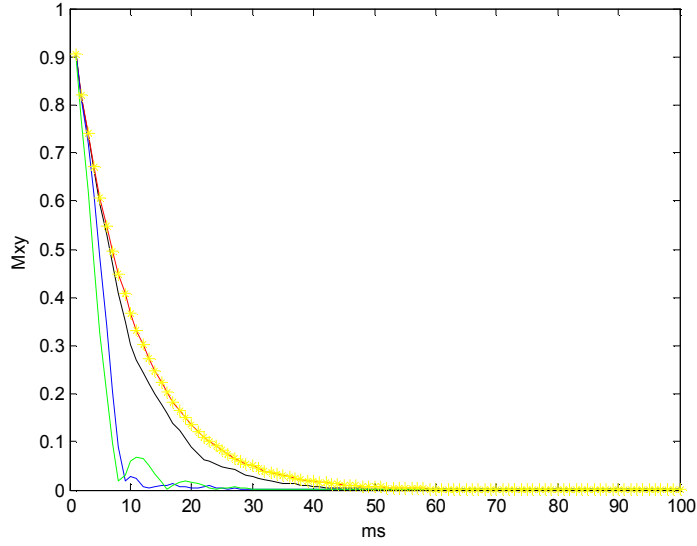
Figure 7. Signal decay to validate motional narrowing effect. Yellow: static
dephasing regime without linear gradient field, green: static dephasing regime with
linear gradient field, red: normal diffusion without linear gradient field, black:
normal diffusion with linear gradient field, and blue: slow diffusion with linear
gradient field. The pass probability was 100%.

To validate that the simulation model was working well in GRE and spin echo
(SE) sequences, simulations were performed for each sequence in 100% pass
probability. The results demonstrate that the GRE signal with ω of the
perpendicular fiber decayed faster than that in the parallel fiber (Figure 8). On the
other hand, in SE, the signal decay with ω in the perpendicular fiber became the
same as that with ω in the parallel fiber at echo time (TE) (Figure 9), confirming
that the developed simulation model was working well in the conventional MRI
sequences.

12
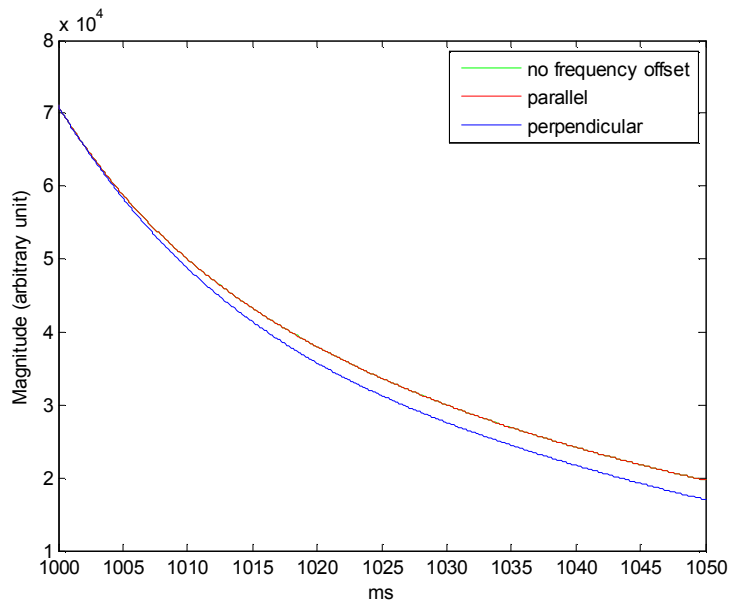
Figure 8. Signal decay from GRE in parallel (red) and perpendicular (blue) fibers.

The pass probability was 100%.
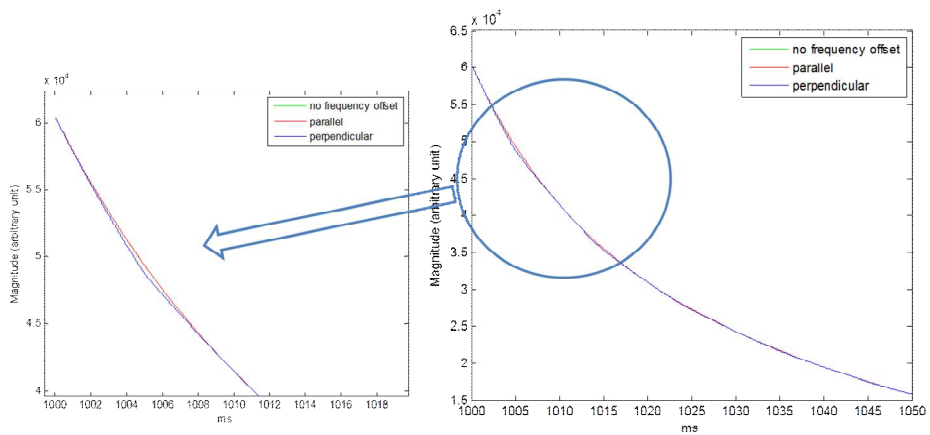
Figure 9. Signal decay from SE in parallel (red) and perpendicular (blue) fibers.

Left figure is the magnified figure of right figure. The pass probability was 100%.

2.2.3 Data Analysis

For ViSTa, the study used the same parameter as the literature (TI_1 = 560 ms, $T1_2$ = 220 ms, TD = 380 ms, and repetition time (TR) = 1160 ms, (7)). For GRE, the study used the same TR of 1160 ms as ViSTa. After 90° excitation, the ViSTa and GRE signals were fitted to a single exponential curve to investigate dominant T_2^*. The phase of ViSTa and GRE was calculated at 10 ms after excitation.

To validate that the ViSTa signal is from myelin water, the study investigated the ViSTa signal changing myelin water residence time (i.e. pass probability in this study). We investigated the residence time until 5000 ms.

2.3 Results

The simulation results are summarized in Figures 10 and 11. The ViSTa signal shows T_2^* of 10 ms when the myelin water residence time is over 118 ms. On the other hand, T_2^* of GRE is independent of the resident time over 30 ms (Figure 10). Regarding the phase evolution, the ViSTa signal shows a positive phase evolution of above 0.6 rad after 118 ms of the myelin water residence time while GRE has almost 0 rad phase (Figure 11).
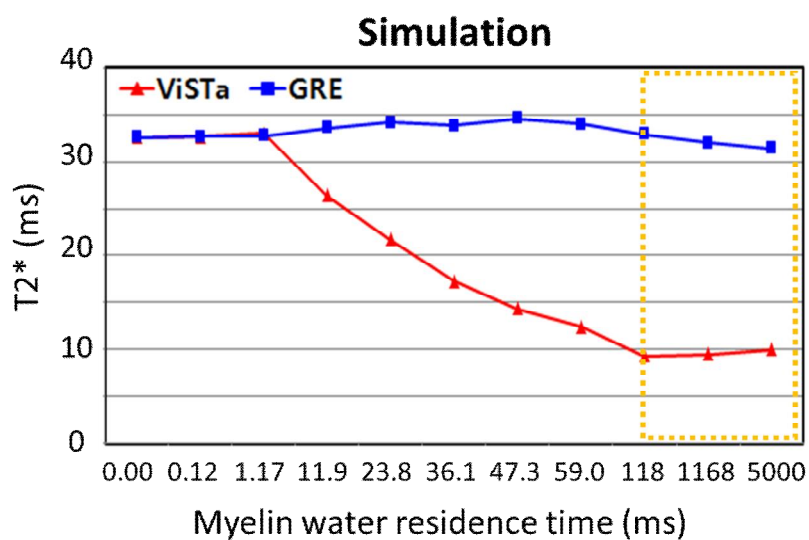
Figure 10. T_2^* fitting results of ViSTa and GRE signals as a function of myelin

water residence time
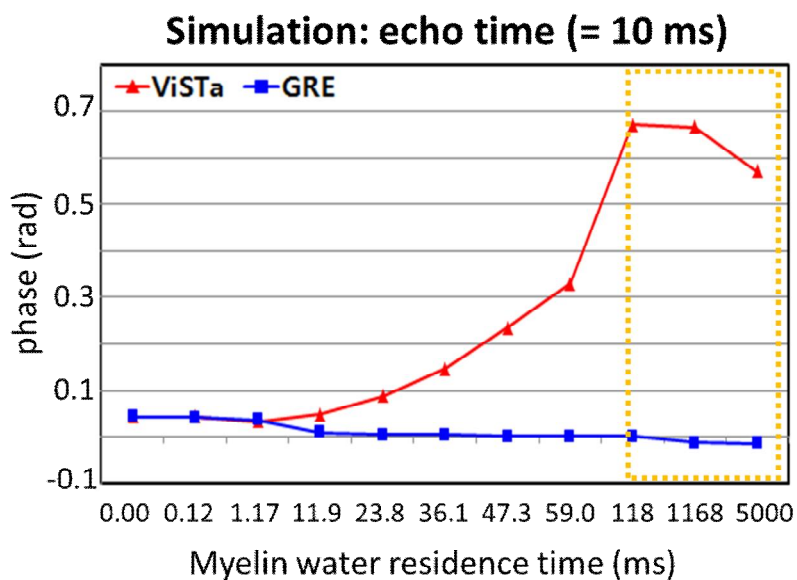
Figure 11. Phase results of ViSTa and GRE signals at 10 ms as a function of myelin

water residence time

15

2.4 Discussion

This chapter demonstrated that the ViSTa signal can have short T_2^* and positive phase evolution for the myelin water residence time of 118 ms or longer, agreeing with in-vivo results (7,8). A few previous studies have demonstrated that myelin water residence time is around or larger than 100 ms (14,15), which is in agreement with this simulation result. Therefore, the study supports the idea that the ViSTa signal originated from myelin water.

Chapter 3. Blood Flow Simulation Model

3.1 Introduction

In ViSTa MWI, artifacts from the inflow of blood have been shown to be a primary source for image degeneration. In the previous works (7-9,11-13), a flow saturation pulse was utilized to reduce the artifacts. However, the inflow of blood still generated ghost artifacts as shown in Figure 12. In this chapter, the effects of inflow have been analyzed by computer simulation and a new flow saturation scheme, which provides robust inflow blood signal suppression, to improve the robustness of ViSTa MWI.
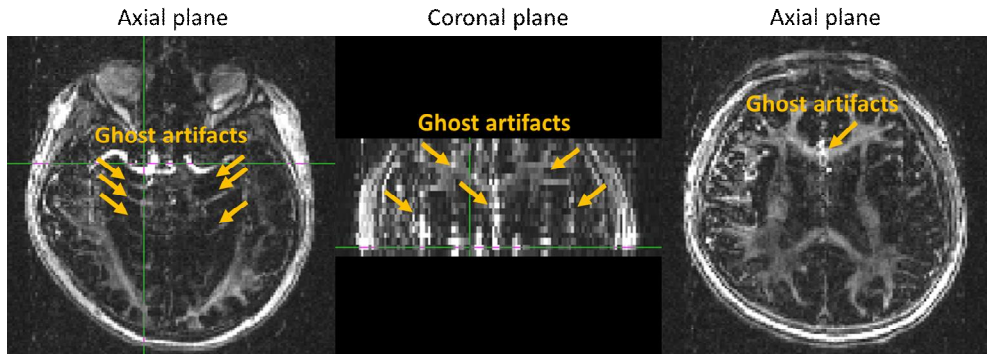
Figure 12. Ghost artifacts in ViSTa image due to inflow of blood

3.2 Methods

3.2.1 Flow Saturation Pulse

A flow saturation pulse suppresses the unwanted blood signal from the outside field of view to reduce inflow-induced artifacts. As shown in Figure 13, a slice selective 90° pulse, the saturation pulse, is transmitted to the saturation band to flip magnetizations into the transverse plane. Then, strong spoiler gradients along phase and frequency encoding directions are applied to induce phase dispersion of the magnetizations. The transverse signal at TE is suppressed because of the phase dispersion of the magnetizations.
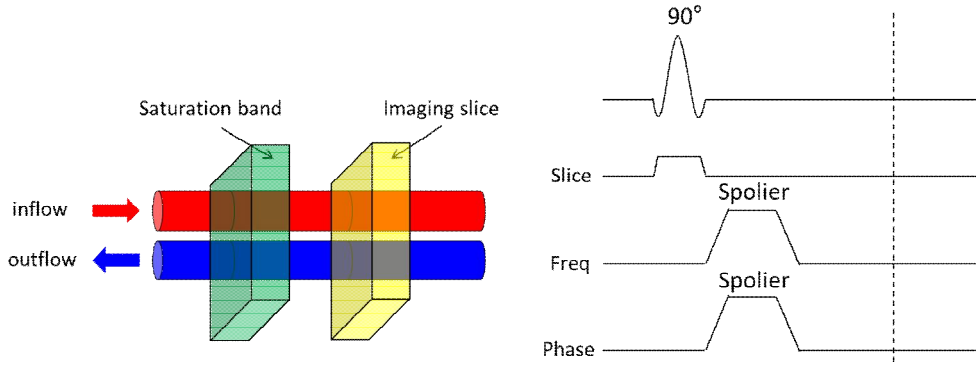
Figure 13. Flow saturation pulse

3.2.2 Simulation Model

To analyze the inflow-induced effects and to calculate the optimal timing of flow saturation pulses, computer simulation was developed. The simulation was conducted under several conditions as summarized in Figure 14.

Simulation model	Condition	Measurement

• Velocity of blood flow
   - Blood pressure
   - Types of vessels
 	
• Structure
	• Velocity
	
	• Phase of BP
	
	• Timing of flow sat.
		• Coverage in ROI
		
		• Suppressed magnitude in ROI

Figure 14. Diagram of flow simulation

For the computer simulation, the following assumptions were made. Instant blood flow velocity was assumed to be proportional to blood pressure. Blood pressure was set to be normal blood pressure; systolic and diastolic blood pressures were 120 mmHg and 80 mmHg, respectively.

Based on the literature (16), the simulation considered different velocities for carotid artery and cerebral artery. The normal range of carotid artery was assumed to be in the range of mean 25 – 65 cm/sec (0.25 – 0.65 mm/ms) (17). The velocity of cerebral artery was assumed to be one-fourth of that of carotid artery (16).

Normalization and scaling of blood pressure were performed. For the normalization, the intensity of blood pressure as a function of time was divided by the first intensity of blood pressure. Then, the normalized intensities of blood pressure were scaled to make that an average of the intensities over some period of time was set to be the mean velocity of blood flow.

The brain model for the simulation is shown in Figure 15. Lengths of

saturation band and the brain were 110 mm and 100 mm, respectively. Carotid artery was placed in saturation band and cerebral artery was placed in the brain. The simulation assumed carotid artery and cerebral artery were aligned in one line from saturation band to the brain. Cerebral vein was not included in this simulation since region of interest (ROI) for blood suppression did not include cerebral vein. Magnetization-saturated blood in the saturation band went up at a velocity of blood flow that changed with respect to the regions.
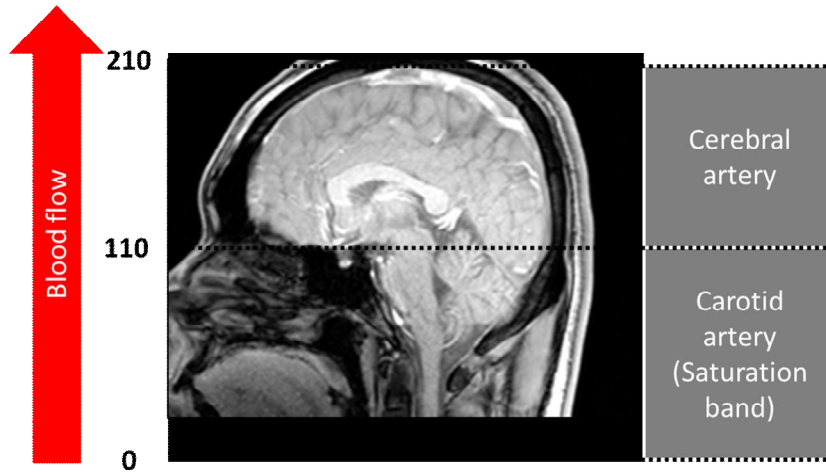
Figure 15. Structure of simulation

At the time of image acquisition (i.e. TE), the phase of blood pressure can be different. To incorporate this phase variation, the simulation was conducted for different phases with an interval of 10 ms.

To decide the optimal timing of flow saturation pulse(s), a grid search was performed between 50 to 780 ms with an interval of 20 ms (Figure 16).
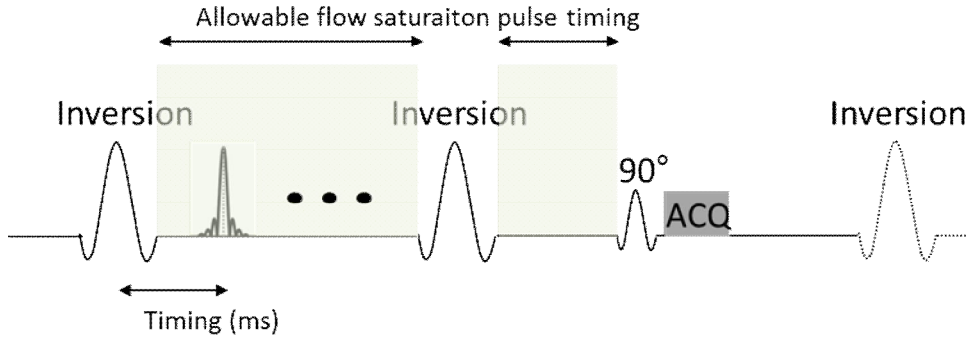
Figure 16. Positioning of flow saturation pulse in ViSTa diagram

To generate the level of inflow suppression, an ROI, which was 55 mm to include middle cerebral artery, was set just above saturation band.

To decide the optimal timing, coverage and suppressed magnitude of saturated blood in ROI were calculated in the simulation. The simulation assumed that water protons were placed from 0 to 210 mm with a 0.01 mm interval (i.e. the number of water protons in the saturation band was 11000 and the number of water protons in ROI was 5499). The water protons moved up to the top of the brain at the velocity of blood flow depending on carotid or cerebral artery until the imaging time (TE). If a flow saturation pulse was applied at a certain time (t_c), saturated protons of 11000 in the saturation band were moving up to the brain from t_c to TE. Then, coverage and suppressed magnitude at TE were calculated using the top and bottom locations of moving blood saturated. Coverage was calculated by a ratio of the number of saturated protons within the ROI to the number of protons in ROI and suppressed magnitude (%) was as follows.

$$\frac{\left(1 - \left(1 - e^{-(TE - t_c)/T1_{blood}}\right)\right) \times S_p}{T_p} \times 100$$

where T_{1blood} is 1550 ms, t_c is flow saturation timing, S_p is the number of saturated protons in ROI, and T_p is the total number of protons in ROI (n = 5499). If an inversion RF pulse is applied after t_c, the signal magnetization recovered until inversion was inverted and then continued to experience magnetization recovery.

3.2.3 Validation

Figure 17 shows coverage and suppressed magnitude in ROI after one flow saturation pulse at an example timing of 540 ms. In ROI, a total number of protons is 5499. After the flow saturation pulse, the simulation estimated coverage ratio of 79%, the sum of suppressed magnitude of 3813, and suppressed magnitude ratio of 69%. Mathematically, coverage ratio was {156.6 (a highest location of suppressed water proton) – 113.3 (a lowest location of suppressed water proton)} / 55 (length of ROI) = 79%. Sum of suppressed magnitude was 0.8805 (recovered magnitude) * 4331 (number of suppressed water proton in ROI) = 3813. Then, coverage ratio was 3813 / 5499 * 100 = 69%. All mathematical results were the same as the simulation results.
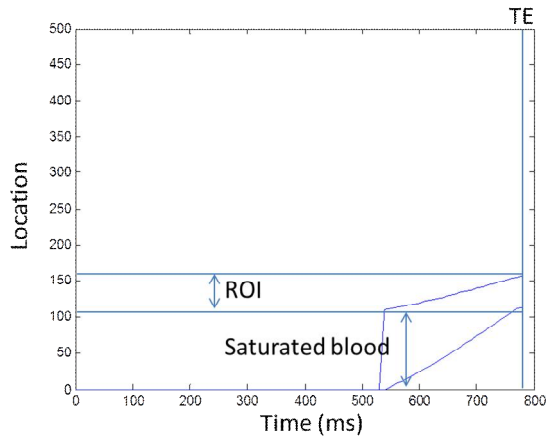
Figure 17. One flow saturation pulse at 540 ms and location of moving protons

3.2.4 Optimal Timing

In human, the velocity of blood flow for carotid artery is wide, ranging 0.25 mm/ms to 0.65 mm/ms. Hence, this study determined the optimal timing of a flow saturation pulse to be robust in a wide range of blood flow velocity for clinical use. The optimal timing of the flow saturation pulse was determined based on the minimum coefficient of variation (COV) of suppressed magnitude. COV was calculated by a standard variation of suppressed magnitude between velocities by a mean suppressed magnitude between velocities. To consider the different phase of blood pressure, the suppressed magnitude was averaged over the different phase of blood pressure.

3.2.5 Analysis

This study calculated the optimal timing according to the different number of flow saturation pulses. For investigation of the effects of difference conditions on

23

suppressed magnitude obtained from the optimal timing, variation of blood pressure (high: 150/100 mmHg and low: 90/60 mmHg), heart rate (fast: 150 per minute and slow: 50 per minute), and B_1 (80 and 120% inhomogeneity) was applied to the simulation. Based on the proposed optimal timing, ViSTa MWI with one flow saturation pulse was applied to two in-vivo subjects.

3.3 Results

3.3.1 Original ViSTa

Figure 18 shows the suppressed magnitude signal of original ViSTa (one flow saturation pulse at 300 ms) with respect to the velocity of carotid artery. When the mean velocity is faster than 0.5 mm/ms, the magnitude suppression level is less than 10%, confirming that original ViSTa may not suppress flow signal in subjects with the high velocity of blood flow.
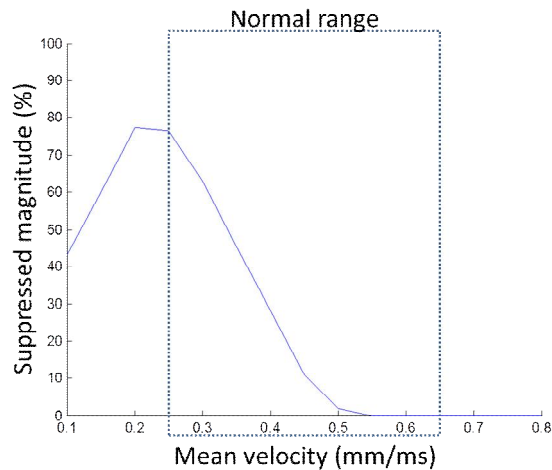
Figure 18. Suppressed magnitude of original ViSTa according to velocity of carotid artery

3.3.2 Optimal Timing for Flow Saturation Pulse

When one flow saturation pulse was used, the computer simulation results suggest that the optimal timing was 530 ms (Figure 19). The mean and standard

deviation of suppressed magnitude in the normal range (carotid artery: 0.25 to 0.65 mm/ms) were 59.1 and 9.0%, respectively. The resulting COV was 15.3%. The mean and standard deviation of coverage were 67.7 and 10.3%, respectively with COV of 15.3%.

Suppressed magnitude

Coverage of flow sat.

FS1 = 530 ms
Mean = 59.1, Std = 9.0
CoV(%) = 15.3

FS1 = 530 ms
Mean = 67.7, Std = 10.3
CoV(%) = 15.3
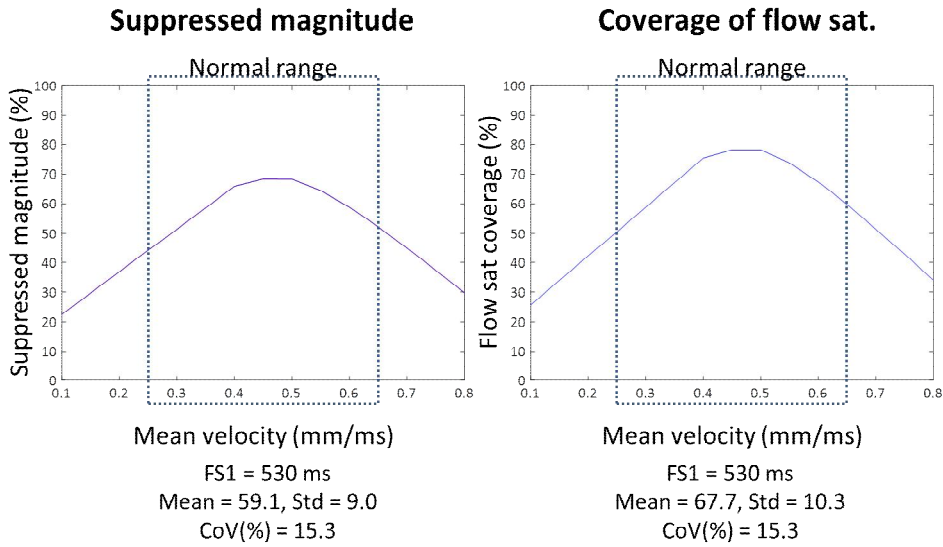
Figure 19. Suppressed magnitude and coverage of one flow saturation pulse with optimal timing according to velocity of carotid artery

3.3.3 Different Conditions of Simulation

Figure 20 shows suppressed magnitude of an optimal timing in high and low blood pressure, fast and slow heart rate, and 80 and 120% B_1 inhomogeneity.

Regarding blood pressure, the difference of mean suppressed magnitude from normal pressure was 5.6 and 4% in high and low pressure, respectively. When heart rate was investigated, the difference of mean suppressed magnitude from

normal heart rate was 8.2 and 10.2% in fast and slow heart rates, respectively.

B_1 inhomogeneity induced errors of 0.8 (80% B_1 inhomogeneity) and 18% (120% B_1 inhomogeneity) suppressed magnitudes from normal B_1.
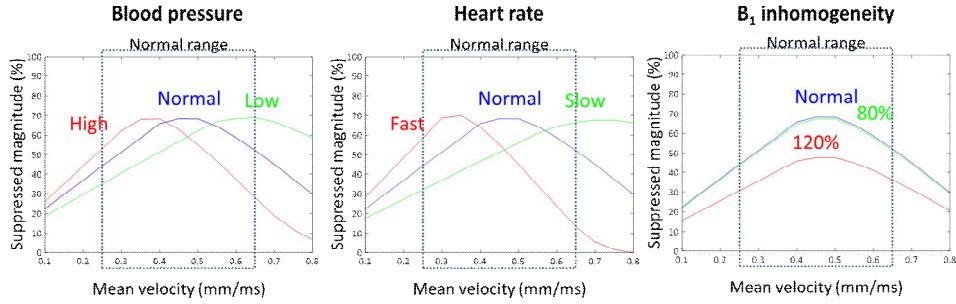
Figure 20. Suppressed magnitude of one optimal timing in high and low blood pressure (left), fast and slow heart rate (center), and 80 and 120% B_1 inhomogeneity (right)

3.3.4 In-vivo Results

Figure 21 shows in-vivo results of ViSTa with one flow saturation pulse. ViSTa with the optimal timing of 530 ms suppressed blood signal more than that with 100 ms and original timing (Figure 21A). On the other hand, the ViSTa image with the optimal timing was similar to that with the original timing in the other subject (Figure 21B). The results demonstrate the limitation of single RF saturation, suggesting two or three RF saturation pulses to improve inflow saturation.
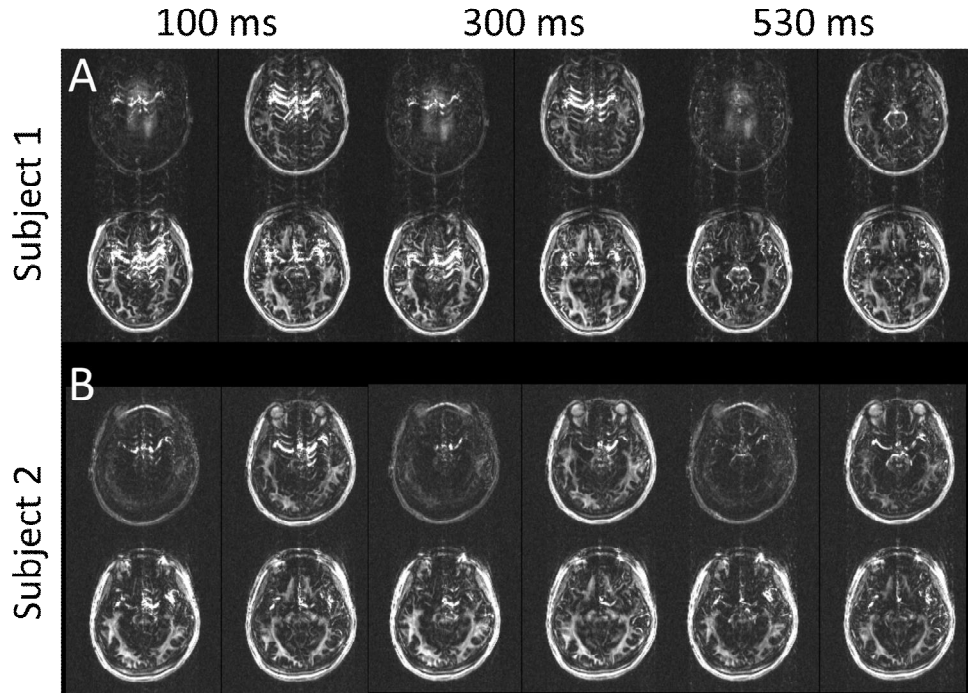
Figure 21. In-vivo results of ViSTa with one flow saturation pulse (100 ms, 300 ms, and 530 ms) for subject 1 (A) and subject 2 (B)

3.3.5 Additional Flow Saturation Pulses

Further investigation was conducted to explore the effects and optimal timings for two and three flow saturation pulses using the same computer simulation.

The resulting optimal timings of two flow saturation pulses were 370 and 610 ms. As shown in Figure 22, the mean and standard deviation of suppressed magnitude in the normal range were 82.8 and 8.7%, respectively with COV of 10.5%. The mean and standard deviation of coverage were 90.0 and 8.6%, respectively with COV of 9.4%, demonstrating improvement over the single RF saturation results.

The optimal timings of three flow saturation pulses were 290, 510, and 650 ms. As shown in Figure 23, the mean and standard deviation of suppressed magnitude in the normal range were 91.2 and 1.9%, respectively with COV of 2.0%. The mean and standard deviation of coverage were 99.0 and 2.3%, respectively with COV of 2.3%, demonstrating improvement over the single or double RF saturation results.
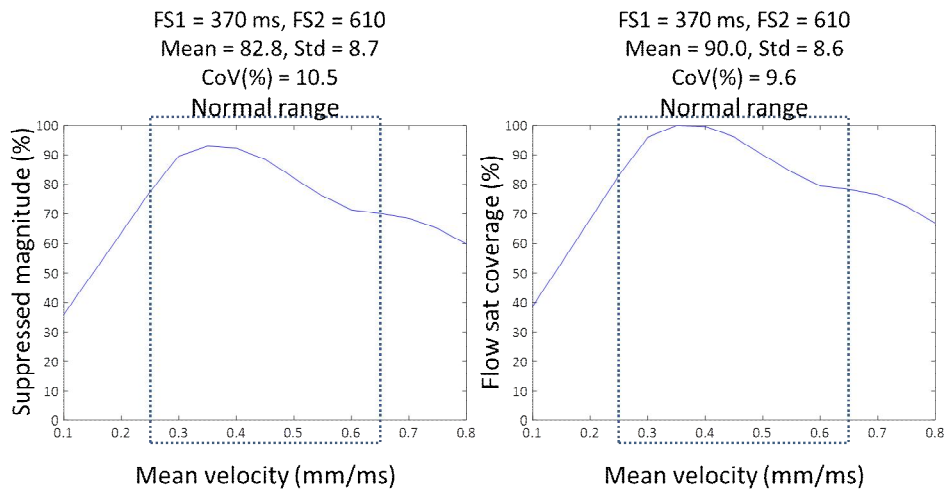
Figure 22. Suppressed magnitude and coverage of two flow saturation pulses with optimal timings according to velocity of carotid artery

FS1 = 290 ms, FS2 = 510, FS3 = 650
Mean = 91.2, Std = 1.9
CoV(%) = 2.0

FS1 = 290 ms, FS2 = 510, FS3 = 650
Mean = 99.0, Std = 2.3
CoV(%) = 2.3
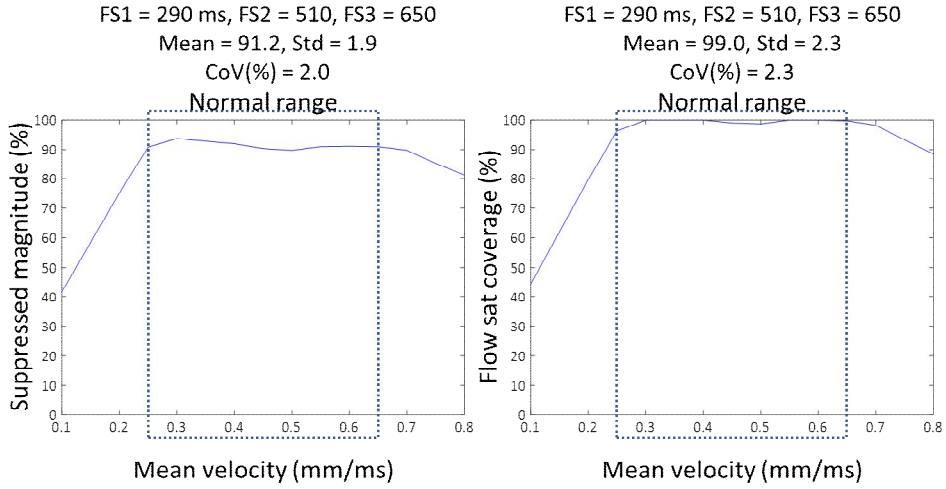
Figure 23. Suppressed magnitude and coverage of three flow saturation pulses with optimal timing according to velocity of carotid artery

3.4 Discussion

In this chapter, I explored the optimal timing of a flow saturation pulses to suppress flow signal in ViSTa MWI. The simulation results suggest the optimal timing that may provide high inflow signal suppression level in the various velocities of blood flow. Since blood velocity is not easily measured or known, two or three flow saturation pulses may demonstrate more robustness in various velocities than one flow saturation pulse. However, stimulated echo from multiple flow saturation pulses may induce errors additionally.

Another approach of reducing ghost artifacts from blood flow is phase correction after image acquisition. Navigator echo may be one possible approach for the phase correction. The phase difference between lines of k-space data due to

the inflow of blood can be compensated.

This study has several limitations. First, this study simplified the structure of blood vessels. The study calculated the location of blood flow assuming carotid artery and cerebral artery was aligned in one line. This may induce a difference between reality and the simulation. Second, this study did not consider magnetization transfer effects. More flow saturation pulses may cause bigger magnetization effects. Due to magnetization effects, MWF could be slightly changed. However, magnetization effects occur normally at very high flip angle (about 2000°). The flip angle of the flow saturation pulse in this study was 90°.

In conclusion, new ViSTa with the suggested optimal timing is expected to reduce flow artifacts in ViSTa image and to utilize for clinical research.

Chapter 4. Clinical Applications

In this chapter, I investigated the white matter characteristics of three prominent brain diseases and injury using ViSTa MWI. To utilize ViSTa MWI in the clinical studies, a summary of new data analysis pipelines for ViSTa MWI and clinical results are presented in this chapter. Three subchapters consist of MS (Chapter 4.1), NMOSD (Chapter 4.2), and TBI (Chapter 4.3) studies.

4.1 Multiple Sclerosis

4.1.1 Introduction

Multiple sclerosis (MS) is a chronic inflammatory disease of the central nervous system characterized by demyelination and axonal loss (18). Conventional T_1 and T_2 weighted images have been used to identify MS lesions that often appear as T_1 hypointensity and T_2 hyperintensity signals in white matter (WM). Despite obvious contrasts between MS lesions and normal-appearing brain tissue on the conventional images, direct interpretation of MR images such as the lesion count or volume has not shown a strong correlation with clinical disability (19,20), suggesting that there exist other areas of the brain, such as normal appearing white matter (NAWM) and gray matter, that may be affected by this disease (21).

In histopathological studies, the NAWM in MS has shown substantial abnormalities including inflammation, microglial activation, gliosis, demyelination,

32

and axonal swelling (22-25). These changes have been detected by advanced MR imaging approaches including quantitative T_1 or T_2 measurements (26,27), diffusion tensor imaging (DTI) (28-30), magnetization transfer imaging (MTI) (31,32), and MWI (31,33-35). Interestingly, the abnormalities in the NAWM have been observed even before the formation of a visible lesion (36,37) and have been shown to have a correlation to clinical disability (33,34). It has also been used to understand the pathogenesis of MS (32). Therefore, a method that can reliably detect changes in the NAWM can be an important tool for exploring MS.

MWI is a method that measures myelin water signal in the myelin sheath (5). Recently, the new ViSTa MWI has been proposed to overcome the limitation of low image quality of the conventional MWI. This new method uses double inversion preparation to suppress long T_1 signals from axonal and extra-cellular spaces. As described in Chapter 1.3, ViSTa signal has been validated to have characteristics of myelin water.

In this subchapter, we investigated the applicability of ViSTa MWI for the detection of the reduced myelin water signal in the NAWM of MS. For comparison, gradient echo and spin echo (GRASE) MWI was acquired. Additionally, statistical powers and minimum sample sizes were calculated for both MWIs in global and regional brain areas.

4.1.2 Methods

4.1.2.1 Study Participants

This study was approved by the Institutional Review Board. Forty-three

subjects, who provided written consents, participated in the study. Twenty-five MS patients were enrolled in the outpatient clinic. For comparison, 18 HC subjects were also recruited from among associates or family members of the patients. Student's t-test and Chi-square test were performed to confirm no significant differences in age and gender between the groups, respectively (p = 0.66 for age and p = 0.77 for gender). For the MS patients, the median expanded Disability Status Scale (EDSS) score (38) was 2.0 with a range of 0 to 6.5, and the mean disease duration was 6.0 ± 4.9 years. The characteristics of the groups are summarized in Table 3. No patient was on steroid pulse therapy for at least one month prior to the scan.

Table 3. Characteristics of MS patients and healthy controls

Variable	MS	Healthy Controls	*P* Value
No. of subjects	25	18	NA
Age (y)*	33.8 (20 – 46)	35.7 (25 – 50)	.66
Men : women	10 : 15	7 : 11	.77
Median EDSS score*	2.0 (0 – 6.5)	NA	NA
Disease duration (y)*	6.0 (.4 – 18.5)	NA	NA

NA = not applicable. * Numbers in parentheses are ranges.

4.1.2.2 MRI Protocols

Data were acquired using a 32 channel phased-array head coil with a 3T MRI (Trio, Siemens, Erlangen, Germany). All scans were acquired in the axial plane. To

identify lesions, the following clinical scans were performed: (a) T_1 weighted 2D spin echo imaging (TR, 550 ms; TE, 9.2 ms; flip angle, 70°; pixel dimensions, 0.8 × 0.7 mm^2; number of slices, 32); (b) T_2 weighted 2D turbo spin echo imaging (TR, 8750 ms; TE, 90 ms; echo train length, 21; pixel dimensions, 0.5 × 0.5 mm^2; number of slices, 32), and (c) 2D T_2 fluid attenuated inversion recovery sequence (FLAIR) imaging (TR, 9000 ms; TE, 87 ms; inversion time, 2500 ms; echo train length, 16; pixel dimensions, 0.7 × 0.7 mm^2; number of slices, 32). All slices were 3.2 mm thick with a 0.8 mm gap between the slices.

For the GRASE MWI, a modified 3D GRASE sequence (39) was acquired (TR, 1000 ms; echo train length, 32; first echo time, 10 ms; echo spacing, 10 ms; pixel dimensions, 1.5 × 1.5 × 4 mm^3; number of slices, 28; echo-planar imaging (EPI) factor, 3; scan time, 14 min. 5 sec.). A few subjects were scanned with a longer TR and echo spacing due to the SAR limit.

For the ViSTa MWI, a 3D segmented EPI based ViSTa sequence (7,40) was implemented using the following parameters: TR, 1160 ms; TE, 5.5 ms; TI_1, 560 ms; TI_2, 220 ms; TD, 380 ms; flip angle, 90°; pixel dimensions, 1.5 × 1.5 × 4 mm^3; number of slices, 32; EPI factor, 15; scan time, 6 min. 53 sec. Flow and fat saturation pulses were included to remove flow and fat artifacts. The ViSTa scan was repeated to match the scan time with that of the GRASE MWI. No substantial motion was observed between the scans and, therefore, the two images were averaged without registration. To quantify the ViSTa MWF, a proton density weighted gradient echo (PD GRE) sequence based on the same segmented EPI structure as the ViSTa sequence was acquired with a shorter TR (TR, 75 ms; scan

time, 30 sec.). Two different flip angles (28° for MWF analysis and 5° for image registration of the ViSTa MWI) were acquired. The total scan time for the two ViSTa and two PD GRE scans was 14 min. 46 sec.

4.1.2.3 Data Processing

To estimate the MWF of the GRASE MWI, the T_2 distribution of the water signal (ranging from 10 to 2000 ms) was calculated using a regularized nonnegative least-square fitting method (5) followed by stimulated echo correction (39,41). Myelin water was defined as the signals from 10 to 40 ms. The MWF of the GRASE MWI was calculated as a ratio between the sum of the myelin water signals and the sum of the entire T_2 distribution.

To quantify the ViSTa data, the signal fraction was calculated by dividing the ViSTa data by the PD GRE data (flip angle with 28°) and multiplying a scaling factor (following equation, (7)).

$$\left(1 - e^{-\frac{TR}{T_{1GRE}}}\right) * \sin(FA_{GRE}) / (1 - e^{-\frac{TR}{T_{1GRE}}} * \cos(FA_{GRE}) \quad * \ e^{\left(-\frac{TE}{T_{2} \cdot GRE}\right)} / e^{\left(-\frac{TE}{T_{2} \cdot ViSTa}\right)}$$

The scaling factor compensated for the TR and flip angle differences between the GRE and ViSTa and the T_2^* decays in the GRE and ViSTa using nominal values (T_1 of the GRE signal = 800 ms, T_2^* of the GRE signal = 40 ms, and T_2^* of the ViSTa signal = 10 ms) as suggested in the literature (7). This nominal value correction has little effect on the MWF estimation of the NAWM but may introduce errors in the MWF estimation in lesions (see 4.1.4 Discussion). The

resulting ViSTa MWF was referred to as an apparent MWF (aMWF) due to the limited information about the scaling factor (7). When compared to the MWF of the GRASE MWI, the aMWF of the ViSTa MWI was approximately one third.

4.1.2.4 Data Registration

For mask generation and quantitative evaluation, intra-scan registration was performed between the acquired images. To generate a mask, the T_1 weighted and FLAIR images of each subject were co-registered to the T_2 weighted images using FMRIB's Linear Image Registration Tool (FLIRT) in FSL (Oxford, UK; (42)) after skull extraction using Brain Extraction Tool (BET) in FSL. For quantitative analysis, the 1st echo image of the GRASE data was co-registered linearly to the T_2 weighted image. Then, the registration matrix was applied to the GRASE MWF map. The ViSTa aMWF map, which was generated using the PD GRE data with a flip angle of 5°, was co-registered linearly to the T_2 weighted image. Then, the registration matrix was applied to the ViSTa aMWF map created by the PD GRE data with a flip angle of 28° using ApplyXFM in FSL.

4.1.2.5 Global White Matter Mask

A global WM mask excluding lesion-appearing voxels was generated as follows: first, an initial mask was created by dividing the registered T_1 weighted image by the T_2 weighted image. This T_1 over T_2 image produced a less biased image from B_1 inhomogeneity and an improved contrast between gray and white matters. The resulting image was segmented to generate a WM mask using

37

Automated Segmentation Tool (FAST) in FSL (43). Then, the lesion-appearing voxels identified in the FLAIR images were removed from the WM mask. To automatically identify the voxels in the FLAIR images, a histogram of the intensity of the FLAIR image was fitted to a Gaussian curve, and voxels with values greater than one standard deviation from the mean of the FLAIR image were labeled as lesion-appearing voxels (Figure 24). These voxels were removed from the mask, generating a final global WM mask with no lesions. The global WM mask was manually inspected to confirm that no lesion-appearing voxel was included in the mask (Figure 25).
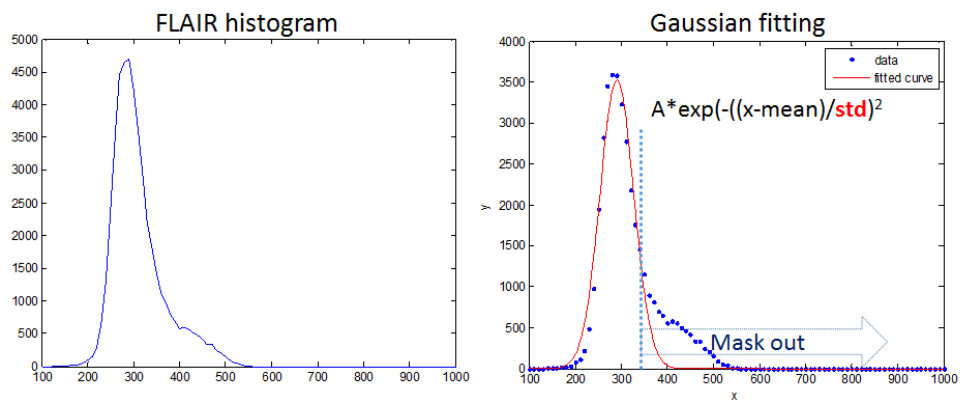
Figure 24. Histogram of FLAIR image (left) and Gaussian fitting to remove lesion-appearing voxels (right)
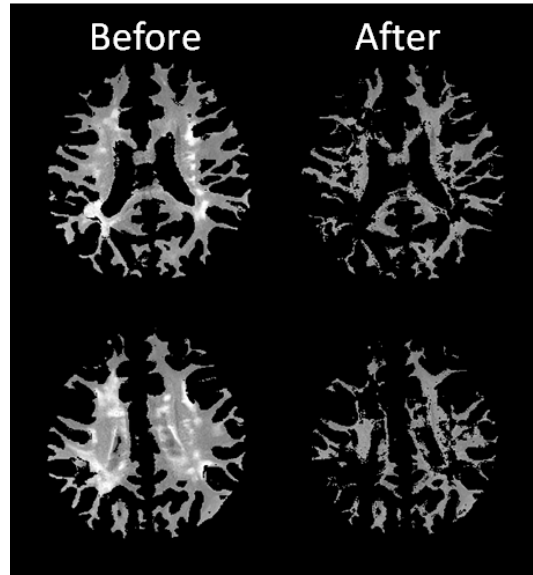
Figure 25. Representative results of removing lesion-appearing voxels in FLAIR

images

4.1.2.6 Regional Normal-appearing White Matter

In addition to the global WM mask, regional WM masks were also drawn using 'roipoly' function in MATLAB. The regions of interest (ROIs) were manually delineated on the centrum semiovale (CS), periventricular WM (PVWM), genu (GN) and splenium (SPL) of the corpus callosum, and optic radiation (OR) shown in Figure 26. The lesions identified in the FLAIR images were excluded from the ROIs. The ROIs were used as regional WM masks. A few patients had lesions at the locations of the ROIs and were excluded for the ROIs. The number of global and regional masks is summarized for MS and HC in Table 4.
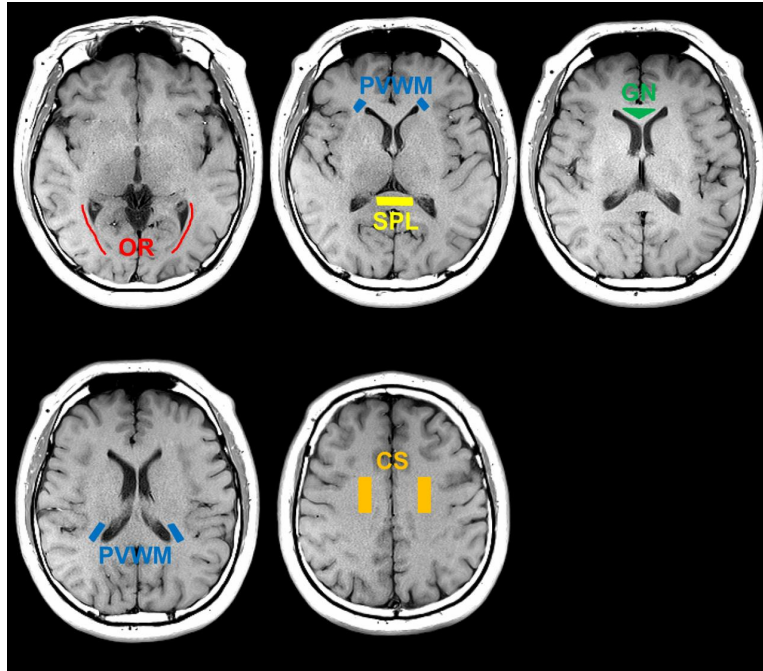
Figure 26. Example of regions of interest on T_1 weighted image. OR: optic radiation, PVWM: periventricular white matter, SPL: splenium of corpus callosum, GN: genu of corpus callosum, CS: centrum semiovale (CS)

Table 4. Number of global and regional masks study cohorts

	MS Patients	Healthy Controls
Global white matter	25	18
Centrum semiovale	34	36
Periventricular white matter	32	70
Genu of corpus callosum	20	18
Splenium of corpus callosum	24	18
Optic radiation	24	36

4.1.2.7 Data Analysis

The ViSTa aMWF and GRASE MWF of the NAWM in the MS patients were compared with those of normal WM (NWM) in HC in the global and regional WM masks using a general linear model adjusted for age and gender. The statistical powers and minimum sample sizes required for a statistically significant difference between the MS patients and HC were calculated for each mask for both MWIs. The statistical power and the minimum sample size were obtained using the 'pwr.f2.test' function in the R program (RStudio Inc., Boston, USA). The age and gender were used as covariates for the power and sample size calculation.

In addition to the analysis of all the MS patients, the ViSTa aMWF and GRASE MWF of early-stage MS patients (disease duration < 2 years) were compared with those of the HC using a general linear model adjusted for age and gender. The early-stage MS patients were selected from the study population.

To assess the clinical relevance of the NAWM MWF in the MS patients, Spearman's correlation coefficients were calculated between the MWF and EDSS score and the MWF and disease duration. Additionally, Spearman's correlation coefficient was calculated between the ViSTa aMWF and GRASE MWF to demonstrate the similarity between the two MWIs. All the correlation analyses were performed for the global WM mask.

Additional analysis for MS lesion was performed. ViSTa aMWF in lesions with T_1 enhancement by contrast agent (Gadolinium) were compared to that in lesions without T_1 enhancement. The lesion with T_1 enhancement is an active lesion with inflammation while that without T_1 enhancement is a chronic lesion. All

chronic lesions were drawn in the same slice as the active lesions.

The Statistical Package for the Social Sciences version 21.0 (SPSS Inc., Chicago, IL, USA) was used to conduct the general linear models and the correlation analyses. A p-value threshold (< 0.05) was deemed to indicate statistical significance.

4.1.3 Results

Representative FLAIR, T1 weighted, ViSTa aMWF, and GRASE MWF images for a HC and a MS patient are shown in Figures 27 and 28, respectively. The ViSTa aMWF images reveal a superior image quality compared to the GRASE MWF images.
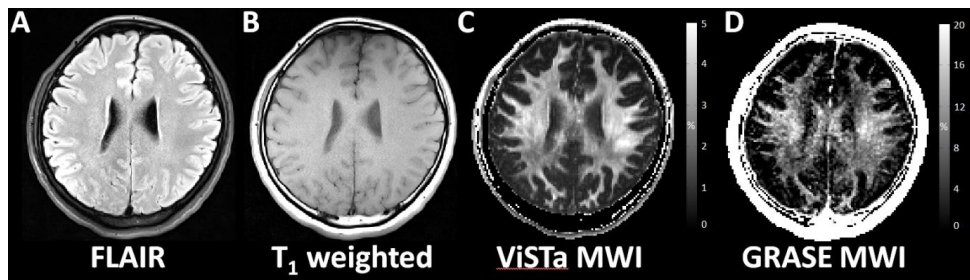
Figure 27. Representative FLAIR (A), T1 weighted (B), ViSTa aMWF (C), and GRASE MWF (D) images from a 32-years-old healthy female.
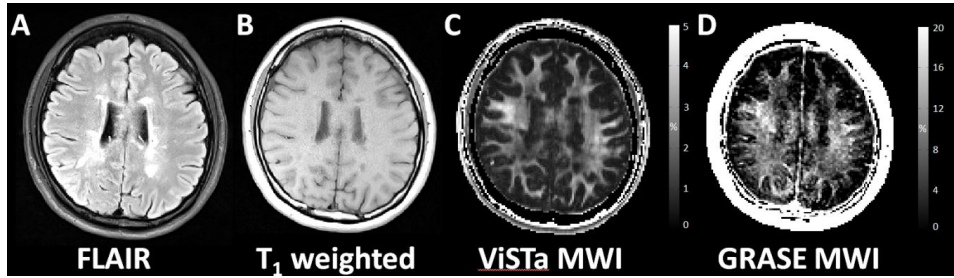
Figure 28. Representative FLAIR (A), T1 weighted (B), ViSTa aMWF (C), and GRASE MWF (D) images from a 24-years-old female MS patient

4.1.3.1 Analysis of MWF in Global and Regional Masks

The mean MWFs of the global and the regional WM masks in the MS patients and HC are summarized in Table 5. The mean MWFs of the masks in the GRASE MWI (range 6.0 – 12.7% for the MS patients; 7.0 – 14.7% for the HC) are approximately three times higher than those in the ViSTa MWI (range 2.5 – 3.9% for the MS patients; 3.1 – 4.7% for the HC) due to the aforementioned scaling factor.

Table 5. Global and regional myelin water fractions in normal appearing white matter for ViSTa MWI and GRASE MWI

	MWF (%)		
Modality and Location	MS (n = 25)	HC (n = 18)	*P V*alue
ViSTa MWI			
Global WM	2.5 ± .3	3.1 ± .3	<.001
Centrum semiovale	3.0 ± .5	3.4 ± .6	<.001
Periventricular WM	2.6 ± .4	3.1 ± .4	<.001
Genu of CC	3.9 ± .7	4.6 ± .4	<.001
Splenium of CC	3.5 ± .6	4.6 ± .5	<.001
Optic radiation	3.8 ± .6	4.7 ± .5	<.001
GRASE MWI			
Global WM	8.4 ± 1.2	10.0 ± 1.3	<.001
Centrum semiovale	11.2 ± 3.0	12.3 ± 4.2	.06
Periventricular WM	6.0 ± 2.4	7.0 ± 2.6	.05
Genu of CC	8.5 ± 4.1	12.1 ± 2.2	.001
Splenium of CC	12.3 ± 4.1	13.8 ± 2.6	.20
Optic radiation	12.7 ± 2.7	14.7 ± 1.8	<.001

Unless indicated, data report means ± standard deviation of MWF. *P* values are derived from a comparison of MWF between MS patients and HC using the general linear model adjusted for age and gender. CC: corpus callosum

When the two groups are compared, the MS patients show reduced MWFs in all regional WM masks (ViSTa MWI: aMWF is reduced by $17 \pm 5\%$; GRASE MWI: MWF is reduced by $16 \pm 8\%$), agreeing with previous studies (on average, 16% in the GRASE MWI (31,34)). In the global WM mask, the MS patients show, on average, a 19% lower aMWF in the ViSTa MWI and a 16% lower MWF in the GRASE MWI compared to those from the HC. These results reconfirm that the WM in the MS patients shows a reduced MWF. Statistically significant differences between the ViSTa aMWFs of the MS patients and the HC are observed in the global and all regional WM masks ($p < 0.001$) (Table 5). On the other hand, the GRASE MWI shows statistically significant differences in the global WM ($p < 0.001$), GN ($p = 0.001$), and OR ($p < 0.001$) while the CS ($p = 0.06$) and PVWM ($p = 0.05$) are slightly above the threshold, and the SPL ($p = 0.20$) is well-above the threshold (Table 5).

To examine the statistical analysis results, the statistical power and the minimum sample size of the two MWI methods were calculated for all masks, and the results are summarized in Figures 29 and 30, respectively. The ViSTa aMWFs show higher powers than those of the GRASE MWFs in all masks (on average, ViSTa aMWF = $99.2 \pm 1.6\%$, and GRASE MWF = $75.5 \pm 31.0\%$; Figure 29). The ViSTa MWI requires a smaller sample size than that of the GRASE MWI for all masks (on average, ViSTa MWI = 18 ± 9, and GRASE MWI = 78 ± 75; Figure 30).
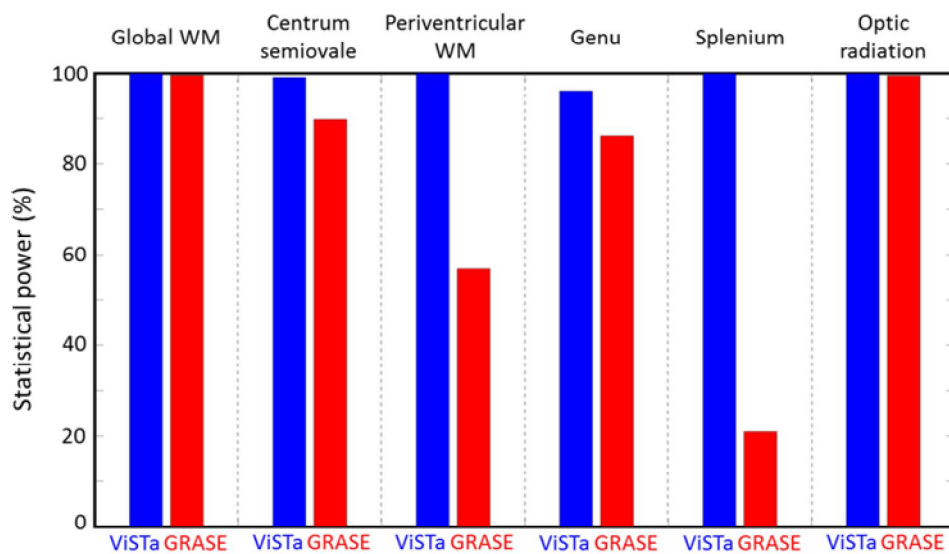
Figure 29. Statistical powers for each ROI
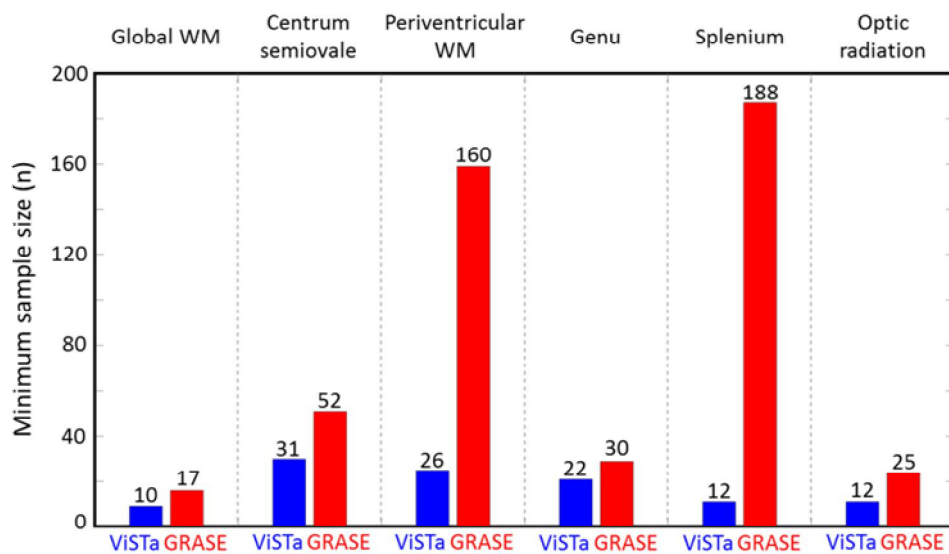
Figure 30. Minimum sample sizes necessary to observe a significant difference

between MWFs of the MS patients and HC

4.1.3.2 Early Stage MS Patients

When the MWFs of the early-stage MS patients (disease duration < 2 years; number of patients = 6) were compared with those of the HC, significant differences between the ViSTa aMWFs of the early-stage MS patients and the HC were found in the global WM and the regional WM masks ($p < 0.01$; Table 6) except for the CS ($p = 0.18$). On the other hand, the GRASE MWI shows a significant difference only in the OR ($p = 0.002$) despite the same trend of reduced MWFs in the early-stage MS patients in all masks.

Table 6. Global and regional myelin water fractions for MS patients with early disease duration (< 2 years) for ViSTa MWI and GRASE MWI

	MWF (%)		
	Early MS	HC	
Modality and Location	(n = 6)	(n = 18)	*P* Value
ViSTa MWI			
Global WM	2.7 ± .3	3.1 ± .3	.004
Centrum semiovale	3.2 ± .7	3.4 ± .6	.18
Periventricular WM	2.5 ± .3	3.1 ± .4	<.001
Genu of CC	3.9 ± 1.0	4.6 ± .4	.009
Splenium of CC	3.6 ± .6	4.6 ± .5	.001
Optic radiation	3.7 ± .3	4.7 ± .5	<.001
GRASE MWI			
Global WM	9.0 ± 1.0	10.0 ± 1.3	.07
Centrum semiovale	10.9 ± 3.3	12.3 ± 4.2	.13
Periventricular WM	6.0 ± 2.4	7.0 ± 2.6	.17
Genu of CC	10.4 ± 4.6	12.1 ± 2.2	.25
Splenium of CC	12.7 ± 4.8	13.8 ± 2.6	.61
Optic radiation	12.7 ± 1.2	14.7 ± 1.8	.002

Unless indicated, data report means ± standard deviation. *P* values are derived from a comparison of myelin water fraction between early-stage MS patients and HC using the general linear model adjusted for age and gender. CC: corpus callosum

4.1.3.3 Relationship between Disease Duration and MWF and EDSS Score and MWF

As shown in Figure 31, the disease duration of the MS patients is significantly correlated with both ViSTa aMWF (r = -0.437 and p = 0.029) and GRASE MWF (r = -0.445 and p = 0.026) in the global WM mask. EDSS scores, however, do not show any correlations (ViSTa aMWF: r = -0.173 and p = 0.409; GRASE MWF: r = -0.171 and p = 0.412; see Figure 32).
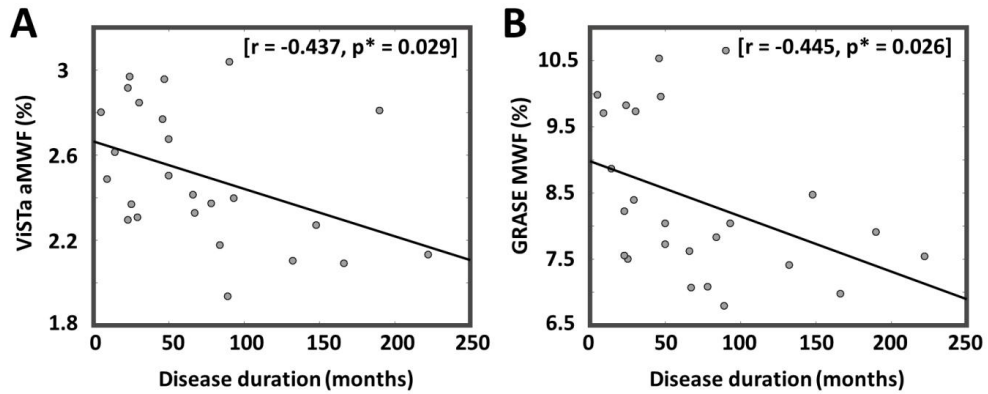
Figure 31. Scatter plots between disease duration and ViSTa aMWF (A) and between disease duration and GRASE MWF (B). aMWF and MWF are values of the global WM mask
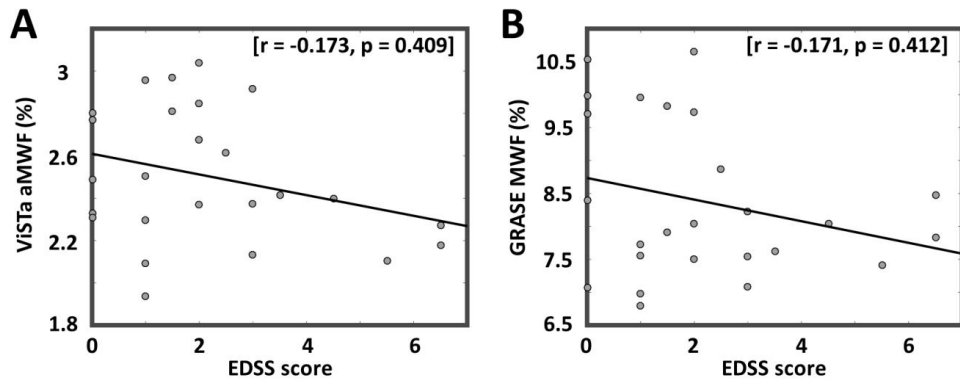
Figure 32. Scatter plots between EDSS score and ViSTa aMWF (A) and between

EDSS score and GRASE MWF (B). aMWF and MWF are values of the global

WM mask

4.1.3.4 Relationship between ViSTa aMWF and GRASE MWF

Figure 33 shows scatter plots between the ViSTa aMWF and GRASE MWF in the global WM mask of the HC and MS patients. The ViSTa aMWF is strongly correlated with the GRASE MWF in both the HC (r = 0.664 and p = 0.003) and MS patients (r = 0.768 and p < 0.001).
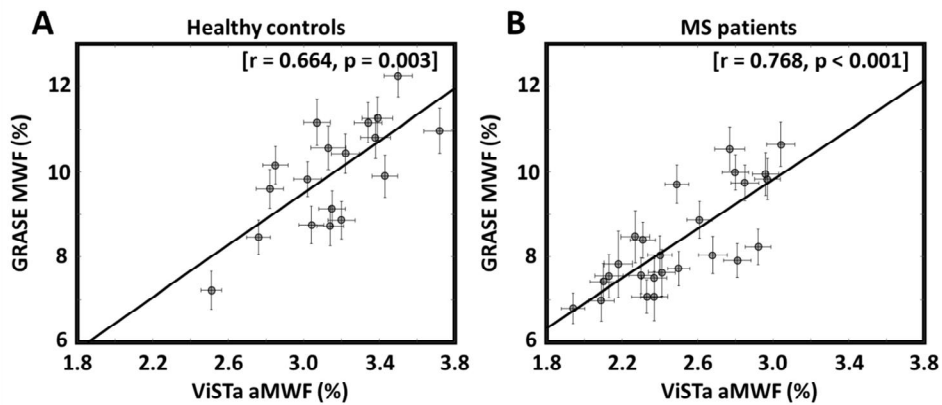
Figure 33. Scatter plots between ViSTa aMWF and GRASE MWF of the global

WM mask in the HC (A) and MS patients (B). ViSTa aMWF is significantly correlated with GRASE MWF. The r and p denote a correlation coefficient and p-value, respectively. Error bars of the scatter plots are 1/10 of the standard deviation

4.1.3.5 MS Lesions

Table 7 shows ViSTa aMWF in active and chronic lesions. aMWF of active lesions was about relatively 67% smaller than that of NAWM in MS when mean aMWF of NAWM was obtained in regional ROIs (Table 5). aMWF of the active lesions was 38% smaller than that of chronic lesions. However, due to the limited number of lesion, the interpretation of the results may be required for further studies.

Table 7. ViSTa aMWF in active and chronic lesions in MS

		Active lesion		Chronic lesion	
Subject	Slice	#voxel	aMWF (%)	#voxel	aMWF (%)
9	19	6	1.18 ± .19	19	1.05 ± .22
17	25	8	.99 ± .15	10	1.93 ± .32
20	10	7	1.22 ± .45	—	—
21	22	7	1.15 ± .14	—	—
26	20, 21	13	.78 ± .08	15	1.43 ± .42

Chronic lesions were drawn in the same slice as active lesions. If there was no chronic lesion in the same slice, this study did not draw ROI for the chronic lesion.

4.1.4 Discussion

In this subchapter, we demonstrated that ViSTa MWI can reliably detect a decreased MWF in the NAWM of MS patients. When compared with the GRASE MWI, the ViSTa MWI provided a substantially higher statistical power than that of the GRASE MWI. The high power in the ViSTa MWI may have helped to detect the reduced MWF in the NAWM of the early-stage MS patients. When the aMWF of the ViSTa MWI was correlated with clinical measures, it showed a significant correlation with disease duration but not with EDSS. When the ViSTa MWI and GRASE MWI were correlated, the results showed high correlations. Hence, our study demonstrates the potentials of ViSTa MWI as a myelin imaging tool for clinical studies.

In the ViSTa MWI, the measure of the myelin water concentration was referred to as the "apparent" MWF because the measurement did not fully compensate for the relaxation parameters (7). The resulting aMWF was approximately one-third of the MWF in the GRASE MWI. When calculating the aMWF, a scaling factor was used to compensate for the effects of the TR, flip angle and T_2^* using the same parameters (T_1: 800 ms for GRE; T_2^*: 40 ms for GRE and 10 ms for ViSTa) suggested in the ViSTa paper (7). Because these parameters were relatively insensitive to the scaling factor, they, therefore, could be applied to calculate the aMWF in the NAWM. For example, T_1 for GRE was shown to be 764 ms in the WM of HC and 792 ms in the NAWM of MS patients (i.e., a 3.5% relative change in T_1) (26), and T_2 (on behalf of T_2^*) for GRE was shown to be 77.7 ms in the WM of the HC and 79.1 ms in the NAWM of the MS patients (i.e., an

approximately 2% relative change in T_2) (44). These differences in T_1 and T_2 (or T_2^*) in the NAWM can cause at most a 2.8% "relative change" in the ViSTa aMWF (e.g., the aMWF changes from 5% to 4.86%). Hence, the nominal values are still adequate for the aMWF estimation of the NAWM. However, further investigation is necessary to fully understand the scaling factors and to match the aMWF to MWF.

One of the interesting results of our study was that the MWF in the OR significantly decreased not only in the total MS patient group but also in the early-stage MS patient group in both the ViSTa and GRASE MWIs. Moreover, the results of the OR have the highest statistical powers among all the regional masks in both MWIs. The reduction of the MWF in the OR was also found in a previous study using track-based spatial-statistics (33). This reduction in the OR may be related to the high incidence of vision problems in MS patients.

The disease duration of the MS patients was significantly correlated with the NAWM MWFs in both ViSTa MWI and GRASE MWI. The results support the possibility of progressive demyelination in the NAWM over a long time period in MS. A recent longitudinal study (45) assessed the NAWM MWF in 11 MS patients (range = 3.2 – 5.8 years) and reported a significant decrease in the NAWM MWF over 5 years, highlighting the possibility of myelin loss over a long time period in the NAWM. Their result corresponds with our result which revealed a significantly negative correlation between the disease duration of the MS patients (range = 0 – 6.2 years) and NAWM MWF. This correlation may suggest slowly progressing underlying pathological processes that may contribute to disease progression over

time.

ViSTa aMWF was significantly reduced in the NAWM of the early-stage MS patients with less than 2 years of disease duration. This result agrees with studies that reported the reduction of T_1 over T_2 contrast or MWF in the NAWM of early-stage MS (46,47). The reliable detection of an aMWF reduction in the ViSTa MWI may help to apply this technique for future early-stage MS research.

This study has a few limitations. For our early-stage MS patient analysis, the study population was small (n = 6); therefore, a further study is necessary to consolidate the findings. For the regional masks, the ROIs were manually drawn to avoid lesions. This may have introduced unexpected biases despite the efforts of impartiality in drawing the masks. Because the whole brain mask, which was automatically generated, showed similar changes to the regional masks, we believe the biases were small. In this study, the GRASE MWF showed no significant decrease in a few regional ROIs in MS. Our expectation, however, is that the GRASE MWI would show significantly reduced MWFs in all regional ROIs if we had a larger number of patients. This expectation is supported by the results of the global WM ROI, which had a larger number of voxels than those of the regional ROIs, and also by a previous MWI study (34) with a larger sample size (33 MS patients and 18 controls), showing significant decreases in the MWF in most of the regional ROIs.

Finally, we want to acknowledge that the biophysical interpretation of the MWF change in the MWI (both ViSTa MWI and GRASE MWI) requires caution because the reduction in MWF does not directly translate into a reduction in myelin

concentration. For example, it has been reported that the myelin water signal does not distinguish between myelin debris and undamaged myelin (48). Moreover, the myelin water fraction can be incorrectly measured for pathological cases including intramyelinic edema (49). Hence, one has to be careful in interpreting myelin water fraction changes. Despite this caution, this method has important potential in exploring white matter changes that are not evident from GRASE MRI as demonstrated in this study. To further validate the use of ViSTa MWI in clinical studies, studies with larger size cohorts may be warranted.

4.2 Neuromyelitis Optica Spectrum Disorder

4.2.1 Introduction

Neuromyelitis optica spectrum disorder (NMOSD) is a neurodegenerative disease and characterized by an anti-aquaporin-4 antibody-mediated astrocytopathy with secondary demyelination (50). NMOSD involves inflammation and demyelination of the optic nerve primarily.

Recent advances in MRI technology have improved the assessment of WM volume loss, cortical thinning, and gray matter damage in various disease states (51-54). To this end, various efforts have been made to improve the detection of occult brain damage in NAWM of patients with NMOSD. However, the results of these studies have been contradictory. Early studies using MTI and magnetic resonance spectroscopy found no differences in the NAWM between the NMOSD patients and control subjects (54-57). In contrast, DTI studies have identified widespread or regional NAWM involvement in NMOSD (58-66); yet, no specific findings have been identified to help distinguish demyelination on advanced MRI sequences. Although DTI is highly sensitive to pathological changes at the microstructural level, it is not specific for individual pathologies such as demyelination. Fractional anisotropy (FA) values, one of DTI parameters have been less specific to myelination. There was no large FA difference between the shiverer mouse and controls (67). Thus, it remains unclear whether subclinical demyelination exists in the NAWM of NMOSD patients. Moreover, it is unknown whether NAWM demyelination is widespread or restricted to visual and motor

pathways in NMOSD.

In the subchapter, the aim was to determine whether changes in NAWM could be detected for NMOSD patients by using both conventional GRASE and ViSTa MWIs, and the presence of subclinical WM change in NMOSD patients with and without brain involvement was evaluated in global WM and in various ROIs. Finally, we analyzed correlations between NAWM abnormalities and clinical variables in order to provide a profile of clinically relevant WM damage in NMOSD.

4.2.2 Methods

4.2.2.1 Study Participants

Twenty-eight patients with NMOSD were prospectively enrolled from the outpatient clinic. Diagnoses of NMOSD were based on the 2015 International Panel for NMO Diagnosis (IPND) (68). All NMOSD patients were seropositive for aquaporin 4 (AQP4) antibody and had not received high dose steroid therapy within one month prior to entering the study. Clinical characteristics including disease duration, history of optic neuritis, and EDSS scores were obtained. All participants provided written informed consent prior to participation. For comparison, the data for 18 age- and gender-matched HC from Chapter 4.1.2.1 were used. Participant characteristics are summarized in Table 8. No statistical differences in age ($p = 0.06$) or gender ($p = 0.2$) were observed between the NMOSD and HC groups although the NMOSD group was slightly older and included more women. The mean disease duration in patients was 11.5 ± 5.5

months and the median EDSS score was 4.0 (range, 0 – 7.5). Of 30 NMOSD patients, 10 had never experienced a brain attack.

Table 8. Characteristics of NMOSD patients and healthy controls

Variable	NMOSD	Healthy Controls	P Value
No. of subjects	28	18	NA
Age (y)	41 ± 10	36 ± 7	.06
Men : women	6 : 22	7 : 11	.2
Median EDSS score*	4.0 (0 – 7.5)	NA	NA
Disease duration (y)*	11.5 ± 5.5	NA	NA

NA = not applicable. * Numbers in parentheses are ranges.

4.2.2.2 MRI Protocol

To obtain images, the same sequences and parameters as the MS study (Chapter 4.1.2.2) were used for this NMOSD study.

4.2.2.3 Data Processing

For the data processing, the same process was performed as the MS study (Chapter 4.1.2.3 – 4.1.2.6) for this NMOSD study. The number of global and regional ROIs is summarized in Table 9.

Table 9. Number of global and regional masks of study cohorts

	NMOSD Patients	Healthy Controls
Global WM	28	18
Centrum semiovale	48	36
Periventricular WM	68	70
Genu of corpus callosum	24	18
Splenium of corpus callosum	23	18
Optic radiation	39	36

4.2.2.4 Statistical Analysis

ViSTa aMWF and GRASE MWF of the NAWM in NMOSD patients were compared with those of the NWM in HC using general linear models adjusted for age and gender.

In addition to the analysis of all NMOSD patients, ViSTa aMWF and GRASE MWF of NMOSD without brain involvement patients were compared with those of HC using a general linear model adjusted for age and gender. The NMOSD without brain involvement patients were selected from the study population.

To assess the association between the NAWM MWF in OR and visual functional system (FS), a partial correlation analysis was used. All statistical comparisons were conducted using the SPSS. P values < 0.05 were considered to indicate statistical significance.

4.2.3 Results

4.2.3.1 Myelin Water Fraction Analyses of Global and Regional NAWM

Figure 34 shows representative images acquired via GRASE and ViSTa MWI. ViSTa images had significantly better image quality and provided better visualization of white matter than conventional images in NMOSD. MWF values are summarized in Table 10. In GRASE MWI, the MWF values of the global NAWM and three ROIs (CS, PVWM, and GN) were slightly lower in the NMOSD patients than in HC subjects; however, these differences were not statistically significant. A significant difference in MWF value was observed in OR of the NMOSD patients relative to HC subjects (12.6 ± 2.1 % vs. 14.7 ± 1.8 %, respectively; p = 0.001). On the other hand, the results of ViSTa analysis revealed a significant reduction of the aMWF values in the global NAWM and several ROIs including CS, PVWM, SPL, and OR in NMOSD patients relative to HC subjects.

To identify subclinical changes in MWF (or aMWF) in NMOSD patients without brain involvement (Table 10), we compared the MWF values of the 10 NMOSD patients who had no brain lesions with those of HC subjects. ViSTa aMWF and GRASE MWF values for OR were significantly lower in the NMOSD patients than in HC subjects (MWF in GRASE MWI: 12.5 ± 2.3 % vs. 14.7 ± 1.8, respectively; p = 0.01; aMWF in ViSTa MWI: 4.1 ± 0.6 vs. 4.7 ± 0.6 %, respectively; p = 0.02).
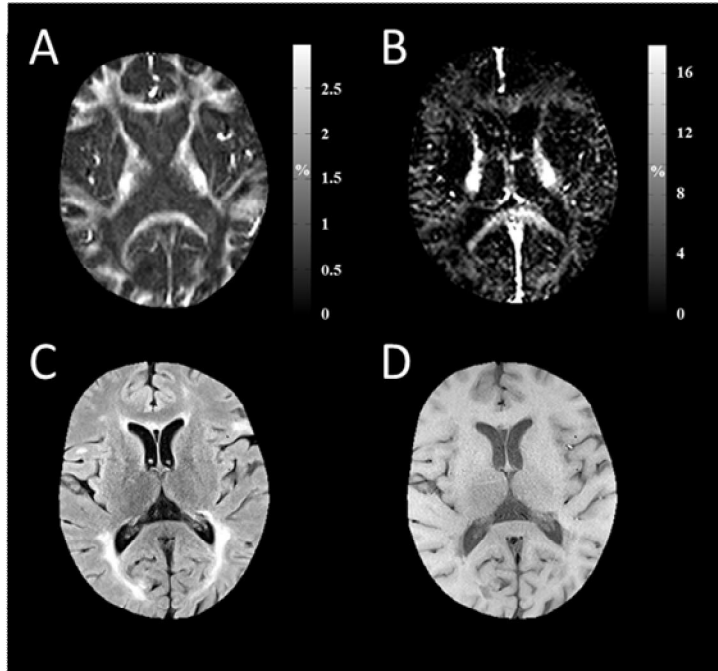
Figure 34. Representative images of ViSTa (A), GRASE (B), FLAIR (C), and T_1 weighted images (D) from a NMOSD patients.

Table 10. Global and regional normal-appearing white matter myelin water fractions for ViSTa MWI and GRASE MWI.

	NMO (n = 28)	NMO w/o (n = 10)	HC (n = 18)	*P* value[1]	*P* value[2]
ViSTa MWI					
Global WM	2.8 ± .4	3.0 ± .3	3.2 ± .3	<.001	.27
CS	3.2 ± .5	3.1 ± .5	3.4 ± .6	.01	.16
PVWM	2.8 ± .5	2.9 ± .5	3.1 ± .4	.03	.23
GN	4.4 ± .7	4.5 ± .5	4.6 ± .4	.16	.69
SPL	4.1 ± .8	4.4 ± .6	4.6 ± .5	.01	.37
OR	4.0 ± .5	4.1 ± .6	4.7 ± .6	<.001	.02
GRASE MWI					
Global WM	9.3 ±1.7	9.5 ± 1.8	9.9 ± 1.3	.12	.52
CS	10.9 ± 3.5	9.5 ± 3.5	12.3 ± 4.2	.09	.17
PVWM	6.8 ± 2.4	7.1 ± 2.0	7.0 ± 2.6	.75	.58
GN	11.5 ± 3.2	11.8 ± 3.0	12.1 ± 2.2	.52	.90
SPL	14.4 ± 4.3	13.8 ± 3.8	13.8 ± 2.6	.99	.91
OR	12.6 ± 2.1	12.5 ± 2.3	14.7 ± 1.8	.001	.01

P value[1] and *P* value[2] derived from the comparison of MWF values between NMOSD and healthy controls, and NMOSD without brain involvement and healthy control using general linear model, adjusting age and gender, respectively. NMO w/o: NMOSD without brain involvement WM: white matter, CS: centrum semiovale, PVWM: periventricular WM, GN: genu of corpus callosum, SPL: splenium of corpus callosum, OR: optic radiation

4.2.3.2 Myelin Water Fraction of Optic Radiation, Optic Neuritis and Visual Function

Because the MWF values of OR were consistently decreased in the NMOSD patients (regardless of brain involvement) on both MWF maps, we further investigated the association between MWF (or aMWF) of OR and visual dysfunction. We compared the mean MWF of OR in the NMOSD patients with and without a history of optic neuritis. Patients with a history of optic neuritis showed lower MWF and aMWF values in OR than patients without a history of optic neuritis (MWF in GRASE MWI: 11.8 ± 2.0 % vs. 14.0 ± 1.8 %, respectively; p = 0.002; aMWF in ViSTa: 3.7 ± 0.4 % vs. 4.4 ± 0.5 %, respectively; p < 0.001; Figure 35). In contrast, we found no difference in MWF of OR between the NMOSD patients without a history of optic neuritis and HC subjects. A partial correlation analysis adjusted for age and gender revealed an association between visual FS score and MWF of OR (GRASE MWI: r = -0.42, p = 0.009; ViSTa MWI: r = -0.44, p =0.007; Table 11).
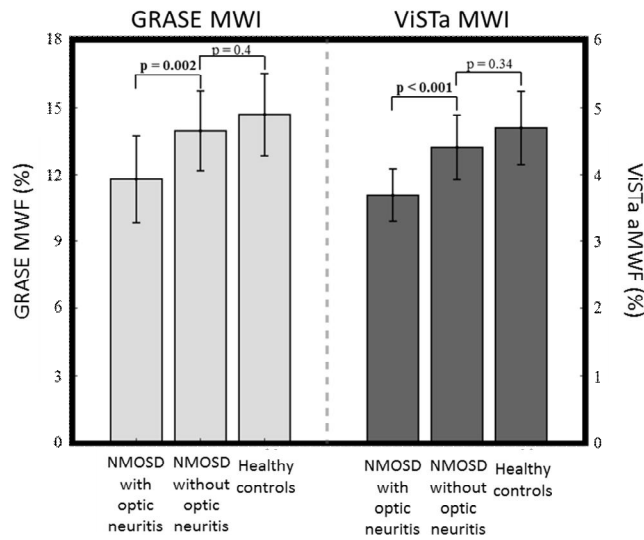
Figure 35. Myelin water fraction in HC and NMOSD with and without a history of optic neuritis. HC: healthy control, NMOSD: neuromyelitis optica spectrum disorder

Table 11. Correlation between visual functional score and myelin water fraction in optic radiation.

	Visual functional score (rho)	*P* value
GRASE MWF	-.42	.009
ViSTa aMWF	-.44	.007

P values derived from the correlation between visual functional score and myelin water fraction using partial correlation analysis, adjusting for age and gender.

4.2.4 Discussion

In this subchapter, we identified widespread changes in the NAWM of NMOSD patients using both conventional GRASE MWI and ViSTa MWI. In parallel analyses, the two MWI maps showed the similar trends of change in the NMOSD patients relative to the HC subjects.

An intriguing finding of this study was that both GRASE MWF and ViSTa aMWF of OR were consistently lower in the NMOSD patients relative to HC subjects. In addition, the NMOSD patients with a history of optic neuritis showed decreased MWF values for OR relative to patients without a history of optic neuritis and relative to HC. Conversely, the NMOSD patients without a history of optic neuritis did not demonstrate a significant difference in MWF of OR relative to HC subjects. Finally, inverse correlations were identified between MWF values of OR (using both GRASE and ViSTa MWIs) and visual FS score. These results are in agreement with a recent DTI study that showed reduced localized FA in OR of NMOSD patients with severe visual impairment relative to those without visual impairment (69). Taken together, these findings suggest that myelin loss in OR may be in part related to direct or trans-synaptic degeneration following optic neuritis and thus reflect visual dysfunction in NMOSD.

Several previous studies reported the restriction of WM damage to OR of NMOSD patients (59,62-65). However, more recent evidence indicates that occult NAWM damage can be present in NMOSD (58,60,61,66). Our finding of a widespread decrease in MWF (or aMWF) in the NMOSD patients is consistent with the latter studies, and suggests that more complex mechanisms may be

involved in the demyelination of NAWM.

In addition, our study showed that reduced MWF in OR also in NMOSD without brain involvement. These results are consistent with a previous study that identified altered WM network connectivity in the absence of discernible WM lesions on T_2 weighted imaging in NMOSD patients (6). Thus, it is reasonable to hypothesize that the disruption of WM integrity can be present even in NMOSD patients who have never experienced a brain attack.

To date, only one study has evaluated MWF of NAWM in patients with NMOSD; however, the study was unable to identify significant differences between the NAWM of NMOSD patients and that of HC subjects using the multi-component Driven Equilibrium Single Pulse Observation of T_1 and T_2 (mcDESPOT) sequence (50). Because NMOSD is an AQP4 antibody-mediated astrocytopathy, NAWM demyelination is not a primary pathology of NMOSD and may, therefore, be difficult to utilize as a clinical prognostic or diagnostic indicator (50). Furthermore, MWF changes in NAWM are far subtler than those in primary lesions in patients with NMOSD (13). We hypothesize that current methods are more sensitive to NAWM change than the previously utilized mcDESPOT. In particularly, ViSTa MWI may be suitable for the early detection of subclinical changes in aMWF in patients with NMOSD.

This study had several limitations. First, we did not include the brainstem in our analysis due to a high propensity for artifacts in the infratentorial area. Because the brainstem is a critical region for evaluating the integrity of the corticospinal tract in NMOSD, this omission may have limited our findings. Similarly, the

posterior limb of the internal capsule, which is frequently involved in patients with NMOSD, could not be evaluated accurately with myelin water (70). Second, although our analysis of patients without brain involvement produced interesting results, the analysis included a rather small number of subjects. Future studies with larger sample sizes are required to confirm our observation of subclinical reduced MWF (or aMWF) in NMOSD patients without brain involvement. Third, the ViSTa sequence has not yet been histologically validated. A pathological-radiological correlation study is warranted to permit the clinical utilization of ViSTa MWI.

In summary, this subchapter identified the presence of widespread changes in the NAWM of NMOSD patients, and in particular highlighted OR as a site of marked decrease in MWF and aMWF. The MWI may offer a direct and potential means for detecting subclinical demyelination in NMOSD.

4.3 Traumatic Brain Injury

4.3.1 Introduction

Traumatic brain injury (TBI) is one of the leading causes of mortality and morbidity worldwide (71). Traumatic axonal injury (TAI), or diffuse axonal injury (DAI), is a hallmark of TBI and is more predictive of behavioral outcome than focal injury in case of moderate to severe TBI (72,73). Because an accurate assessment of the extent of TAI is not currently feasible using conventional T_1- and T_2-weighted images, DTI has been widely used to evaluate WM damage after TBI (74,75). This has represented an important advance in characterizing WM changes associated with TBI. However, DTI is inherently limited in distinguishing among white matter pathologies such as damage to axonal membranes, myelin sheath, or other components of the microstructure (67,76,77).

Myelin has increasingly been considered an important component in the pathophysiology of TBI. Histological studies have demonstrated that TBI induces widespread myelin loss in rat and ex-vivo human brain. Experimentally injured mice have shown significant myelin loss from 3 days to 6 weeks post-TBI compared to sham surgery using electron microscopy (78), and chronic myelin loss is also observed in rats with experimental TBI (79). Histochemical analysis of DAI in post-mortem human brains has also revealed acute myelin loss in WM (80). Accumulating evidence suggests that the myelin loss in TBI may affect neuronal signaling and cognitive function (81,82). Thus, myelin may be an important target for TBI diagnosis, prognosis, and intervention.

Recently, The first human in vivo study using MWI demonstrated a reduction in MWF at 2 weeks post-injury in mild TBI patients (83). However, to be established as a clinically relevant biomarker of myelin damage, reduction in myelin water should be related to injury severity and neurocognitive performance. In this subchapter, we investigated changes in myelin water in moderate to severe TBI using ViSTa MWI (7). Additionally, we examined the clinical relevance of aMWF by assessing its relationship to measures of overall severity of TAI and post-traumatic impairment in cognitive processing speed in patients who sustained moderate to severe diffuse TBI.

4.3.2 Methods

4.3.2.1 Study Participants

Thirty-one adults with moderate to severe TBI were initially enrolled from a specialized inpatient rehabilitation unit. Inclusion criteria were: age between 18 and 64 years old and a diagnosis of non-penetrating moderate to severe TBI as defined by at least one of the following: (1) Glasgow Coma Scale score < 13 in Emergency Department (not due to sedation, paralysis or intoxication); (2) loss of consciousness $\geq$ 12 hours; (3) prospectively documented post-traumatic amnesia (PTA) $\geq$ 24 hours. Participants were excluded for: 1) history of prior TBI, CNS disease, seizure disorder, schizophrenia, or bipolar disorder, 2) history of serious alcohol or psychostimulant (e.g., cocaine) abuse that could have had deleterious neurologic effects, 3) pregnancy, 4) inability to complete MRI scanning due to ferromagnetic implants, claustrophobia, or restlessness, 5) non-fluency in English,

or 6) level of impairment precluding the subject's ability to complete testing and scanning at 3-months post-TBI. To ensure that the TBI was predominantly diffuse, participants were also excluded if the total estimated volume of focal intraparenchymal lesions on acute CT or MRI was greater than 5 cm^3 for subcortical lesions and 50 cm^3 for cortical lesions. Thirty-five HC comparable to TBI subjects in age, gender, and years of education were recruited. Exclusion criteria for HC were the same as above, with the addition of exclusion for any history of TBI resulting in alteration or loss of consciousness. The study was approved by the Institutional Review Board of the home institution and all participants provided written informed consent prior to the participation. Five control and nine patient participants were excluded through after data quality assurance procedures, due to low MR image quality from excessive motion and/or flow artifacts during scanning, and registration failure to a template image for post-processing. As a result, the final analysis included data from 22 TBI and 30 HC. The demographics of these subjects are summarized in Table 12. To confirm that there was no significant group difference, Student's t test was used for age and years of education and Chi-square test was used for gender. The two groups did not differ in age, gender, and years of education. Out of 22 patients, 7 patients did not show any visible focal lesion and only three patients had total lesion volume larger than 20 cm^3, indicating the patients had primarily diffuse pathology.

Table 12. Demographics and mean global values of study cohort

	TBI (N = 22)	HC (N = 30)	Effect size	P value
Age (y)[†]	31.5 ± 13.4	36.5 ± 10.0	.490	.135
Gender (male : female)[‡]	16 : 6	23 : 7	—	.746
Education (y)[†]	14.0 ± 2.3	13.1 ± 2.2	.409	.170
Days post-injury	105.7 ± 21.0	—	—	—
Focal lesion volume (cm[3])	7.7 ± 10.1	—	—	—
aMWF (%)[§]	3.2 ± .4	3.4 ± .3	.769	.049*
FA (%)[§]	47.4 ± 3.0	50.7 ± 1.9	1.727	<.001**
RD[§]	.058 ± .004	.053 ± .003	1.761	<.001**

[†]P values from Student t tests. [‡]P values from Chi-square test. [§]P values from Mann-Whitney U test. *P < .05, **P < .01. aMWF: apparent myelin water fraction, FA: fractional anisotropy, and RD: radial diffusivity.

4.3.2.2 MRI Data Acquisition

Participants with TBI were scanned at 3T MRI (Trio, Siemens, Erlangen, Germany) using an 8-channel phased array head coil.

For ViSTa MWI, a 3D segmented EPI based ViSTa sequence (7) was implemented using the following parameters: TR = 1160 ms; TE = 4.5 ms; in-plane resolution = 1.4 × 1.4 × 5.0 mm^3; number of slices = 26; partial k-space = 6/8, EPI factor = 15; scan time = 7 min 33 sec. Fat and flow saturation pulses were applied

to prevent artifacts from those. To quantify MWF, PD GRE sequence based on the same EPI as the ViSTa sequence was acquired (TR = 97 ms; flip angles = 6° for Figures and 28° for data analysis; each scan time = 38 sec).

A 2D EPI based DTI sequence was acquired (direction = 30; b-values = 0 s/mm2 and 1000 s/mm2; TR = 6500 ms; TE = 84 ms; flip angle = 90°; in plane resolution = $2.2 \times 2.2 \times 2.2$ mm^3; number of slices = 57; scan time = 4 min). To improve signal to noise ratio, DTI was acquired two times and averaged. In addition to MWI and DTI sequences, a routine structural whole brain 3D T_1-weighted magnetization-prepared rapid gradient echo (MPRAGE) was acquired.

4.3.2.3 Data Processing

ViSTa aMWF was calculated by the aforementioned method in Chapter 4.1.2.3. From the DTI data, FA and RD were achieved by using DTIFIT in FSL after eddy current correction.

To investigate statistical group differences between TBI and HC, we generated skeletons of aMWF, FA, and RD. All images including aMWF and FA maps were registered non-linearly to a JHU FA maps using SyN in Advanced Normalization Tools (ANTs) (84,85) after skull extraction of the images using Brain Extraction Tool (BET) in FSL (86). We compared registration quality of SyN, SPM, FSL, and AFNI prior to the following data processing and chose SyN showing the best alignment to a JHU FA map as well as between subjects. For RD maps, RD maps were registered non-linearly to a JHU FA map using warping matrices of FA maps generated in the previous step. To minimize registration error, we generated

Skeletons of aMWF and FA using FSL (87). Skeleton of RD was used the same skeleton as FA. Skeletonization is a method that finds voxels where the location of the voxels with the highest intensity is located at the center of the square (Figure 36).
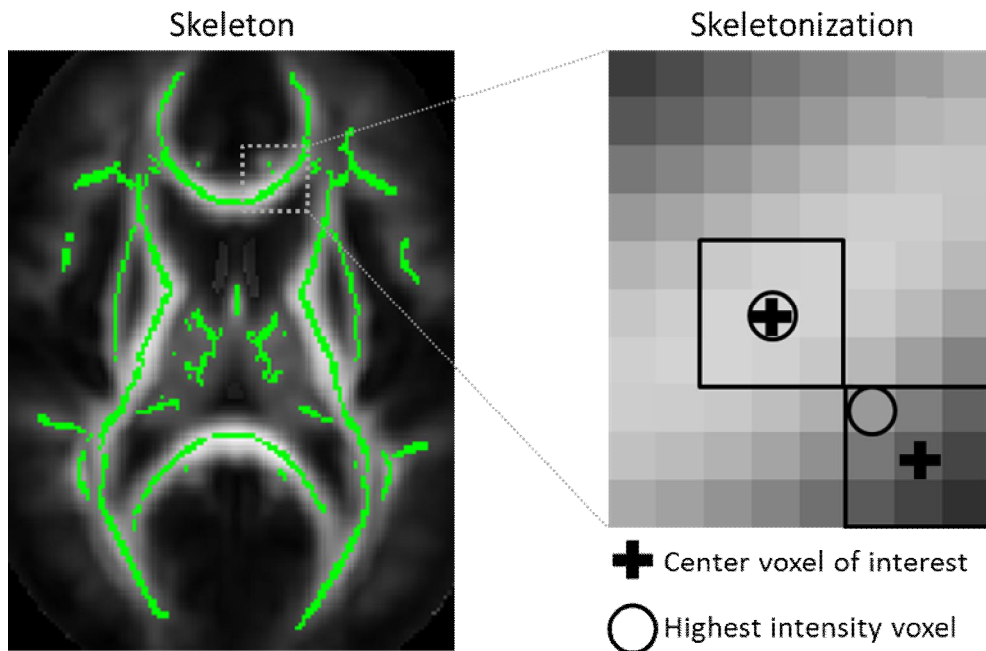
Figure 36. Skeletonization. Skeletonization is a method that finds voxels where the location of the voxels with the highest intensity is located at the center of the square.

4.3.2.4 Clinical Measures

Duration of PTA and cognitive processing speed were evaluated as measures of clinical outcomes. PTA duration, a sensitive index of the severity of neurologic injury, was calculated as the number of days between the TBI and the first of two

occasions within 72 hours that the participant was fully oriented. Full orientation was defined as a score above 25 on the Orientation Log (88), or documentation of consistent orientation for 72 hours in the acute medical record (i.e., prior to rehabilitation admission).

Participants were evaluated at the time of scanning with a neuropsychological battery including measures of attention, verbal learning, executive functioning, and cognitive processing speed. Processing speed was selected for this study a priori because prior work has demonstrated that processing speed measures are sensitive to TBI in general (89), and TBI-related white matter changes in particular (90). For the purpose of the present study, we examined the Processing Speed Index (PSI) from the Wechsler Adult Intelligence Scale IV (91), constructed from age-corrected scores of Digit Symbol and Symbol Search subtests.

4.3.2.5 Data Analysis

For the voxel level group difference between TBI and HC, we performed Tract-Based Spatial Statistics (TBSS) analysis using the skeletons of aMWF, FA, and RD. A two-sample permutation t-test with covariates of age and gender was used by "randomise" in FSL on each voxel of the skeleton (92). Statistical significance was defined by the family-wise error (FWE) rate corrected p value ($<$ 0.05). Additionally, to compare the mean global aMWF, FA, and RD values in TBI with those in HC, all voxels on the skeletons were averaged for each subject. A Mann-Whitney U test was used to evaluate the statistical difference between the groups ($p < 0.05$).

The relationships among three MRI metrics (aMWF, FA, and RD) were examined with Spearman's rank-order correlations. To investigate the clinical relevance of these MRI metrics, Spearman's correlation coefficients were calculated between mean global aMWF, FA, and RD and the duration of PTA and the PSI scaled score. P values < 0.05 were considered to indicate statistical significance. All statistical analyses on global MRI metrics were conducted using the Statistical Package for the Social Sciences version 21.0 (SPSS Inc., Chicago, IL, USA).

4.3.3 Results

Figure 37 shows representative aMWF, FA, and RD images of HC and TBI subjects. The aMWF and FA values in TBI were lower than those in HC in broad areas of the brain. RD values in TBI were also higher than HC in the WM regions, showing widespread WM changes in TBI. Yellow arrows in Figure 37 point to the 'black holes' in conventional DTI images due to crossing fibers (93). However, aMWF shows much less degree of attenuation in those areas, demonstrating MWI's insensitivity to crossing fiber confounds.
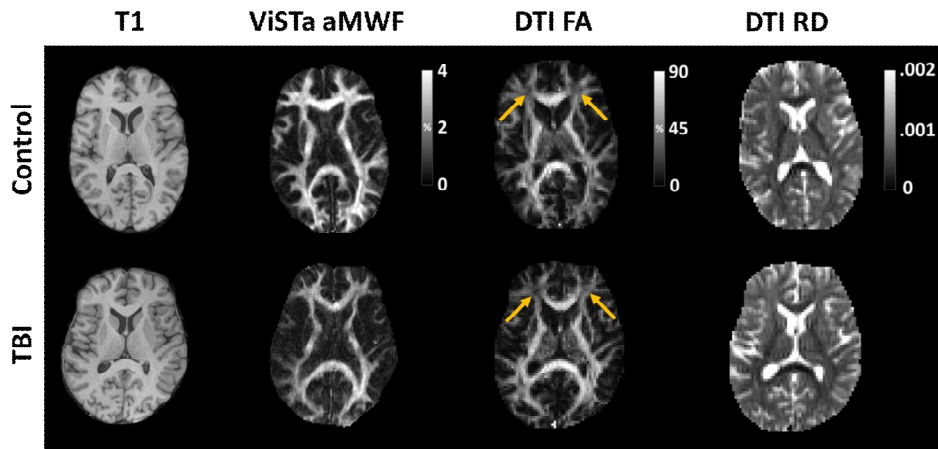
Figure 37. Representative T1 weighted (first column), ViSTa aMWF
(second column), FA (third column), and RD (fourth column) images in a healthy
control (upper row) and a patient with diffuse traumatic brain injury in the absence
of focal lesion (lower row). Arrows point to areas with crossing fibers.

As shown in Figure 38, voxel-wise comparisons of aMWF and FA between
the two groups showed statistically significant widespread reductions in TBI
patients compared to HC ($p < 0.05$) while showing significantly higher RD in TBI
compared to HC, demonstrating that diffuse injury causes spatially substantial
damage to WM.
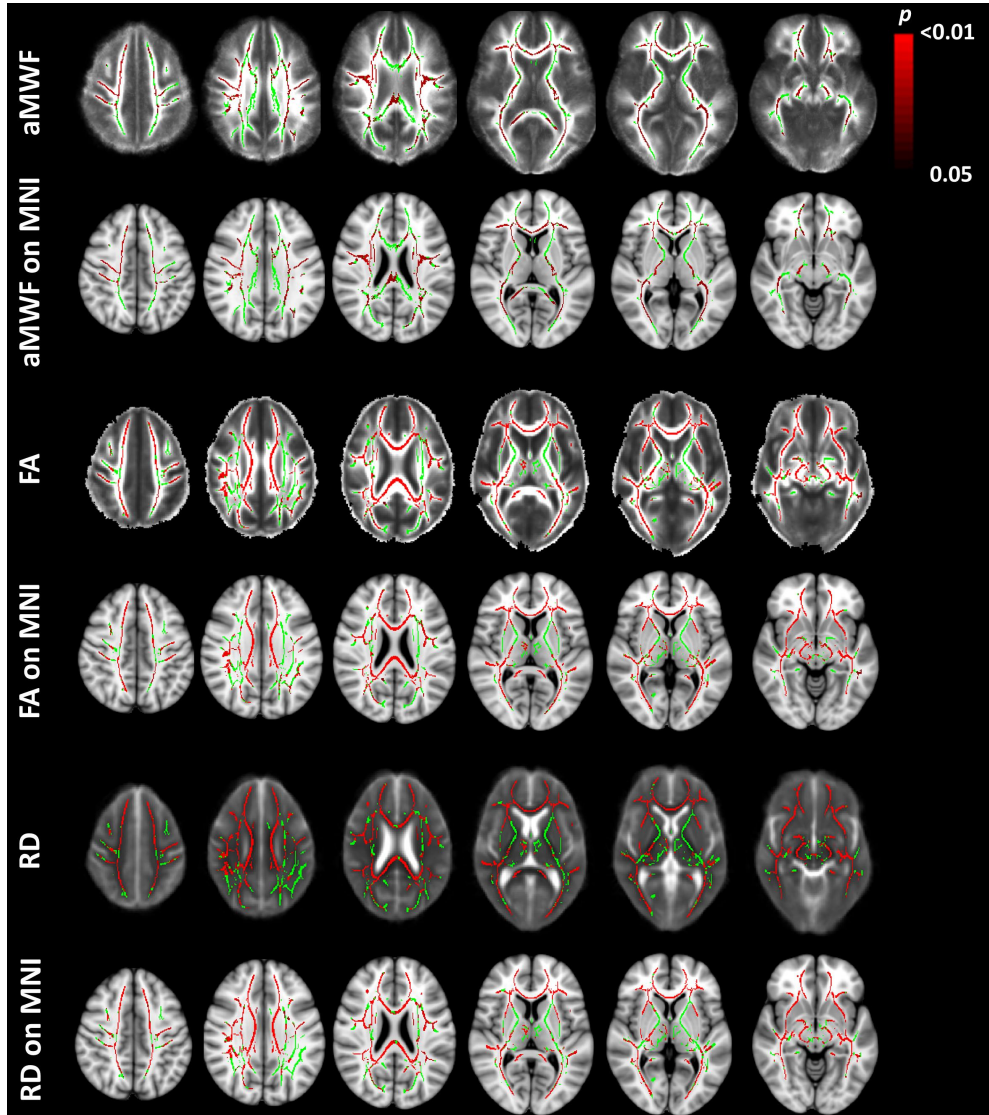
Figure 38. Results of voxel-wise TBSS analysis for comparison of whole brain aMWF (first and second rows), FA (third and fourth rows), and RD (fifth and sixth rows) between TBI patients and healthy controls (p < 0.05. FWE-corrected). Green: skeleton, red: significant voxels. First (aMWF), third (FA), and fifth (RD) skeletons are overlaid on the group template generated for each metric. Second (aMWF), fourth (FA), and sixth (RD) skeletons are overlaid on the MNI template.

Comparing mean global values, the aMWF values in TBI were significantly reduced relative to HC (HC = 3.4 ± 0.3%, TBI = 3.2 ± 0.4%, and p = 0.049) (Table 12). The mean global DTI parameters in TBI were also significantly changed relative to HC (p < 0.001), with the TBI group exhibiting lower FA and higher RD. The effect sizes for group differences between TBI and HC were large for both aMWF and DTI metrics (aMWF = 0.769, FA = 1.727, and RD = 1.761).

To examine the relationship of aMWF with other DTI metrics, Spearman's rank-order correlations were calculated using mean global aMWF, FA, and RD values. Figure 39 shows scatter plots showing the bivariate correlation pattern among the three MRI metrics in HC and TBI groups. While the mean global FA and RD values were highly correlated with each other in both groups (rho = -0.845 for HC, rho = -0.957 for TBI), these DTI metrics were not significantly correlated with aMWF in HC (rho = 0.002 for FA, rho = -0.242 for RD) and only moderately correlated with aMWF in TBI (rho = 0.468 for FA, rho = -0.553 for RD), in agreement with the previous result that DTI metrics may not reflect myelin (67). This pattern of correlation suggests that aMWF may offer complementary information to conventional DTI.
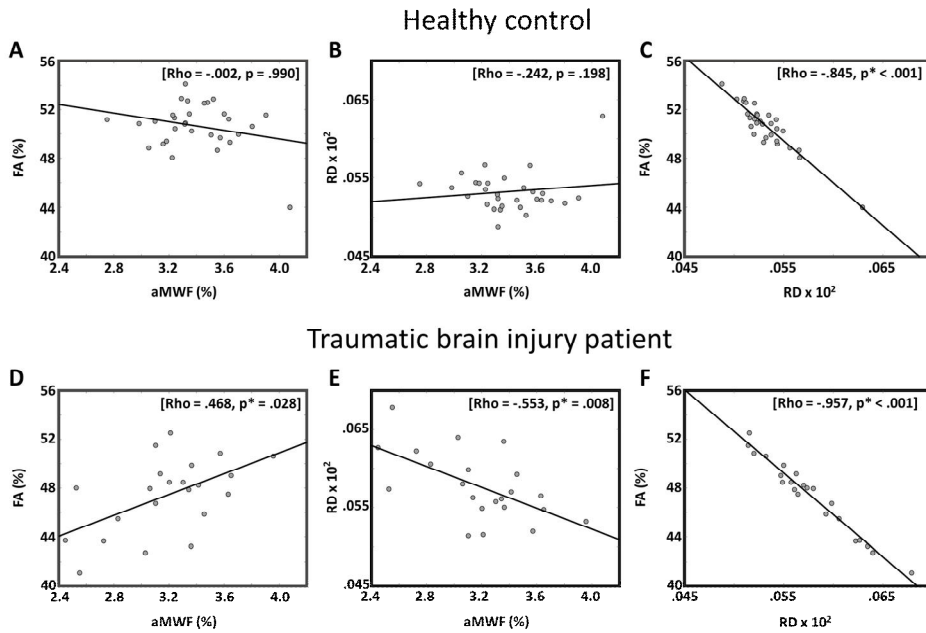
Figure 39. Scatter plots (A, D) between aMWF and FA, (B, E) between aMWF and RD, and (C, F) between FA and RD. (A), (B), and (C) are in HC whereas (D), (E), and (F) are in TBI. Spearman's correlation coefficient and p value, respectively. Asterisk shows significance (p < 0.05).

Regarding the relationship between mean global aMWF, FA, and RD values and clinical outcomes in TBI (Table 13), all three global MRI metrics were significantly correlated with PTA (aMWF; r = -0.564 and p = 0.006, FA; r = -0.647 and p = 0.001, and RD; r = 0.675 and p = 0.001). With regard to PSI, only the correlation with aMWF reached statistical significance (r = 0.452 and p = 0.035). However, given our small sample size, it should be noted that there was also a clear trend toward significant association with DTI metrics (FA; r = 0.405 and p = 0.062 and RD; r = -0.367 and p = 0.092).

Table 13. Spearman's correlation coefficient between MR metrics (aMWF, FA, and RD) and clinical outcomes (PSI and PTA) in TBI.

	aMWF	FA	RD
PSI	.452 (.035)*	.405 (.062)	-.367 (.092)
PTA	-.564 (.006)*	-.647 (.001)**	.675 (.001)**

aMWF: apparent myelin water fraction, FA: fractional anisotropy, RD: radial diffusivity, PSI: processing speed index, and PTA: post traumatic amnesia. *p < .05, **p < .01

4.3.4 Discussion

In this subchapter, we observed widespread changes in myelin water measured by ViSTa MWI in persons with moderate to severe TBI at 3 months post-injury. In a previous MWI study of concussed college hockey players, MWF values were found to recover to a normal level by 2 months post-injury (83). In our cohort, however, the more severe injury appeared to lead to a more persistent reduction in myelin water. Our findings are in line with previous studies that reported the injury to central myelin may contribute to axonal degeneration following TBI over a period of months to several years (94).

We also found that reduced aMWF was proportional to the severity of TAI as estimated by the duration of PTA. This finding supports the notion that MWI may serve as a biomarker to assess the extent of axonal and myelin damage in patients with TAI. We also found that aMWF was significantly correlated with PSI, which suggests that myelin injury may be particularly relevant to processing speed

deficits after TBI. PSI is known as a sensitive behavioral index of the overall extent of diffuse brain injury and is a clinically important phenomenon related to attention, memory, and communication abilities (95). Recent studies have demonstrated that myelinated fibers play a central role in brain messaging and supports processing speed (96). Additionally, studies have reported that myelin thickness is also positively related to signal conduction velocity in the brain (97). Taken together with previous findings, this study strongly suggests that impairment in neural signaling due to moderate to severe brain injury is significantly related to decreases in myelin water.

The relationship among different MRI metrics revealed an interesting pattern. Many researchers have hypothesized that RD indirectly represents the amount of demyelination. However, we found that the correlation between RD and aMWF was only moderate. The fact that aMWF and DTI metrics are only moderately correlated to each other suggests that aMWF may potentially provide complementary information to conventional DTI. As mentioned in the introduction, DTI parameters are affected by various components such as the neurofibrils, axonal membrane, myelin sheath, and intra- and extra-cellular structure in WM (98). Since TBI causes axonal death and increased inter-axonal water where axons and myelin have been lost (99), FA and RD may reflect mixed and accumulated signal changes. Recently, many pieces of evidence have been reported that DTI metrics may not be specific to myelin integrity and may reflect the micro-structural and environmental change of fibers (100,101). The present study employed ViSTa MWI, which is a method that indirectly detects the extent of myelin damage in TBI with high image

quality. Previous studies have demonstrated that MWF is indicative of true changes in myelination (83). Although the acquisition method between ViSTa MWI and conventional MWI is different, many studies have supported that ViSTa aMWF is originated from myelin water (7,8,102,103). Therefore, it is reasonable to conclude that reductions in ViSTa aMWF in our participants with TBI reflect myelin damage due to brain injury.

This study has several limitations that bear noting. First, direct voxel-based comparison of aMWF and DTI metrics could not be done in this study due to the challenge of registering two modalities into a common space. A future study that acquires aMWF and DTI metrics with the same resolution would allow voxel-based comparison between different modalities with minimum registration error. Second, the correlational analysis was based on data from 22 TBI patients. In this small sample, null findings (i.e. lack of significant correlation between PSI and DTI measures) may be due to inadequate power, and hence, should be interpreted with caution. Lastly, the histological study would eventually be needed to clearly elucidate the pathophysiologies contributing to aMWF, FA, and RD. In addition, we examined persons with TBI at a relatively short interval following injury (3 months). It would be of interest to study the clinical correlates, if any, of the imaging measures used in this study at a later point in the recovery process.

For the first time, this study compared aMWF in moderate to severe TBI patients at 3 months post-injury to that in HC. Current results demonstrated reduced aMWF is prevalent in moderate to severe diffuse TBI patients. This implies that TBI causes demyelination of the white matter. Additionally, aMWF

was significantly correlated with measures of injury severity and neurocognitive performance. We believe that aMWF could serve as a potential biomarker for injury severity of myelin and prediction of clinical outcomes.

Chapter 5. Conclusion

The main topic of my thesis is the application of ViSTa MWI to clinical research. To utilize ViSTa MWI, I explored the effects of water exchange and inflow in ViSTa MWI. Then, I developed new data analysis pipelines to apply ViSTa MWI for the clinical studies.

The Monte-Carlo simulation model for myelin water residence time, which was developed in Chapter 2, validated the origin of ViSTa as myelin water. The blood flow simulation model in Chapter 3 suggested the optimal timing of flow saturation pulse(s) to suppress the inflow of blood. The most important part of my thesis is Chapter 4. Chapter 4 summarized new data analysis pipelines for clinical application. Using the analysis pipelines, ViSTa MWI revealed reduced aMWF in normal appearing white matter for three prominent brain diseases and injury: MS, NMOSD, and TBI patients.

The developments in this thesis can be utilized not only in various brain disorders but also in neuro-plasticity studies to explore the answer for the questions related to myelin issues.

References

1.   Wharton S, Bowtell R. Fiber orientation-dependent white matter contrast in gradient echo MRI. Proceedings of the National Academy of Sciences of the United States of America 2012;109(45):18559-18564.

2.   Kalantari S, Laule C, Bjarnason TA, Vavasour IM, MacKay AL. Insight into in vivo magnetization exchange in human white matter regions. Magnetic resonance in medicine 2011;66(4):1142-1151.

3.   Du YP, Chu R, Hwang D, et al. Fast multislice mapping of the myelin water fraction using multicompartment analysis of T2* decay at 3T: a preliminary postmortem study. Magnetic resonance in medicine 2007;58(5):865-870.

4.   Vavasour IM, Whittall KP, Li DK, MacKay AL. Different magnetization transfer effects exhibited by the short and long T(2) components in human brain. Magnetic resonance in medicine 2000;44(6):860-866.

5.   MacKay A, Whittall K, Adler J, Li D, Paty D, Graeb D. In vivo visualization of myelin water in brain by magnetic resonance. Magnetic resonance in medicine 1994;31(6):673-677.

6.   Liu Y, Duan Y, He Y, et al. Altered topological organization of white matter structural networks in patients with neuromyelitis optica. PloS one 2012;7(11):e48846.

7.   Oh SH, Bilello M, Schindler M, Markowitz CE, Detre JA, Lee J. Direct visualization of short transverse relaxation time component (ViSTa). NeuroImage 2013;83:485-492.

8.   Kim D, Lee HM, Oh SH, Lee J. Probing signal phase in direct visualization of short transverse relaxation time component (ViSTa). Magnetic resonance in medicine 2015;74(2):499-505.

9.   Lee HM, Kim D, Oh SS, Choi JY, Oh SH, Lee J. The Phase and Magnetization Transfer Characteristics of a Novel Myelin Water Imaging Method (ViSTa). 23th ISMRM 2014;#338.

10.   Oh SH, Choi JY, Im Y, Prasloski T, Lee J. Myelin Water Fraction of the Whole Brain: 3D GRASE MWI vs. 3D ViSTa MWI. 23th ISMRM 2014;#3143.

11.   Choi JY, Jeong IH, Oh SH, et al. Evaluation of Normal-Appearing White Matter in Multiple Sclerosis Using Direct Visualization of Short Transverse Relaxation Time Component (ViSTa) Myelin Water Imaging and Gradient Echo and Spin Echo (GRASE) Myelin Water Imaging. Journal of magnetic resonance imaging : JMRI 2018.

12.   Jeong IH, Choi JY, Kim SH, et al. Normal appearing white matter demyelination in neuromyelitis optica spectrum disorder. European Journal of Neurology 2017;Accepted.

13.   Jeong IH, Choi JY, Kim SH, et al. Comparison of myelin water fraction values in periventricular white matter lesions between multiple sclerosis and neuromyelitis optica spectrum disorder. Multiple sclerosis (Houndmills, Basingstoke, England) 2016;22(12):1616-1620.

14.   Dortch RD, Harkins KD, Juttukonda MR, Gore JC, Does MD. Characterizing inter-compartmental water exchange in myelinated tissue

using relaxation exchange spectroscopy. Magnetic resonance in medicine 2013;70(5):1450-1459.

15. Deoni SC, Rutt BK, Jones DK. Investigating exchange and multicomponent relaxation in fully-balanced steady-state free precession imaging. Journal of magnetic resonance imaging : JMRI 2008;27(6):1421-1429.

16. Brant WE. The Core Curriculum: Ultrasound. Phiadelphia: Lippincott, Williams & Wilkins: 2001.

17. Bogunovic H, Loncaric S. Blood flow and velocity estimation based on vessel transit time by combining 2D and 3D X-ray angiography. Medical image computing and computer-assisted intervention : MICCAI International Conference on Medical Image Computing and Computer-Assisted Intervention 2006;9(Pt 2):117-124.

18. Keegan BM, Noseworthy JH. Multiple sclerosis. Annual review of medicine 2002;53:285-302.

19. Interferon beta-1b in the treatment of multiple sclerosis: final outcome of the randomized controlled trial. The IFNB Multiple Sclerosis Study Group and The University of British Columbia MS/MRI Analysis Group. Neurology 1995;45(7):1277-1285.

20. Barkhof F. The clinico-radiological paradox in multiple sclerosis revisited. Current opinion in neurology 2002;15(3):239-245.

21. Calabrese M, Favaretto A, Martini V, Gallo P. Grey matter lesions in MS: from histology to clinical implications. Prion 2013;7(1):20-27.

22. Evangelou N, Esiri MM, Smith S, Palace J, Matthews PM. Quantitative pathological evidence for axonal loss in normal appearing white matter in multiple sclerosis. Annals of neurology 2000;47(3):391-395.

23. Geurts JJ, Barkhof F. Grey matter pathology in multiple sclerosis. The Lancet Neurology 2008;7(9):841-851.

24. Kutzelnigg A, Lucchinetti CF, Stadelmann C, et al. Cortical demyelination and diffuse white matter injury in multiple sclerosis. Brain : a journal of neurology 2005;128(Pt 11):2705-2712.

25. Trapp BD, Peterson J, Ransohoff RM, Rudick R, Mork S, Bo L. Axonal transection in the lesions of multiple sclerosis. The New England journal of medicine 1998;338(5):278-285.

26. Vrenken H, Geurts JJ, Knol DL, et al. Whole-brain T1 mapping in multiple sclerosis: global changes of normal-appearing gray and white matter. Radiology 2006;240(3):811-820.

27. Grenier D, Pelletier D, Normandeau M, et al. T2 relaxation time histograms in multiple sclerosis. Magnetic resonance imaging 2002;20(10):733-741.

28. Gallo A, Rovaris M, Riva R, et al. Diffusion-tensor magnetic resonance imaging detects normal-appearing white matter damage unrelated to short-term disease activity in patients at the earliest clinical stage of multiple sclerosis. Archives of neurology 2005;62(5):803-808.

29. Gratsias G, Kapsalaki E, Kogia S, et al. A quantitative evaluation of damage in normal appearing white matter in patients with multiple

sclerosis using diffusion tensor MR imaging at 3 T. Acta neurologica Belgica 2015;115(2):111-116.

30. Werring DJ, Brassat D, Droogan AG, et al. The pathogenesis of lesions and normal-appearing white matter changes in multiple sclerosis: a serial diffusion MRI study. Brain : a journal of neurology 2000;123 (Pt 8):1667-1676.

31. Levesque IR, Giacomini PS, Narayanan S, et al. Quantitative magnetization transfer and myelin water imaging of the evolution of acute multiple sclerosis lesions. Magnetic resonance in medicine 2010;63(3):633-640.

32. Liu Z, Pardini M, Yaldizli O, et al. Magnetization transfer ratio measures in normal-appearing white matter show periventricular gradient abnormalities in multiple sclerosis. Brain : a journal of neurology 2015;138(Pt 5):1239-1246.

33. Kolind S, Matthews L, Johansen-Berg H, et al. Myelin water imaging reflects clinical variability in multiple sclerosis. NeuroImage 2012;60(1):263-270.

34. Laule C, Vavasour IM, Moore GR, et al. Water content and myelin water fraction in multiple sclerosis. A T2 relaxation study. Journal of neurology 2004;251(3):284-293.

35. Oh J, Han ET, Lee MC, Nelson SJ, Pelletier D. Multislice brain myelin water fractions at 3T in multiple sclerosis. Journal of neuroimaging : official journal of the American Society of Neuroimaging 2007;17(2):156-

163.

36.   Filippi M, Rocca MA, Martino G, Horsfield MA, Comi G. Magnetization transfer changes in the normal appearing white matter precede the appearance of enhancing lesions in patients with multiple sclerosis. Annals of neurology 1998;43(6):809-814.

37.   Narayana PA, Doyle TJ, Lai D, Wolinsky JS. Serial proton magnetic resonance spectroscopic imaging, contrast-enhanced magnetic resonance imaging, and quantitative lesion volumetry in multiple sclerosis. Annals of neurology 1998;43(1):56-71.

38.   Kurtzke JF. Rating neurologic impairment in multiple sclerosis: an expanded disability status scale (EDSS). Neurology 1983;33(11):1444-1452.

39.   Prasloski T, Rauscher A, MacKay AL, et al. Rapid whole cerebrum myelin water imaging using a 3D GRASE sequence. NeuroImage 2012;63(1):533-539.

40.   Oh SH, Oh SS, Choi JY, Park JY, Lee J. Three Dimensional Quantitative Myelin Water Imaging using Direct Visualization of Short Transverse Relaxation Time Component (ViSTa). Proc Intl Soc Mag Reson Med 23rd 2014;#4280.

41.   Prasloski T, Madler B, Xiang QS, MacKay A, Jones C. Applications of stimulated echo correction to multicomponent T2 analysis. Magnetic resonance in medicine 2012;67(6):1803-1814.

42.   Smith SM, Jenkinson M, Woolrich MW, et al. Advances in functional and

structural MR image analysis and implementation as FSL. NeuroImage 2004;23 Suppl 1:S208-219.

43.   Zhang Y, Brady M, Smith S. Segmentation of brain MR images through a hidden Markov random field model and the expectation-maximization algorithm. IEEE transactions on medical imaging 2001;20(1):45-57.

44.   West J, Aalto A, Tisell A, et al. Normal appearing and diffusely abnormal white matter in patients with multiple sclerosis assessed with quantitative MR. PloS one 2014;9(4):e95161.

45.   Vavasour IM, Huijskens SC, Li DK, et al. Global loss of myelin water over 5 years in multiple sclerosis normal-appearing white matter. Multiple sclerosis (Houndmills, Basingstoke, England) 2017:1352458517723717.

46.   Beer A, Biberacher V, Schmidt P, et al. Tissue damage within normal appearing white matter in early multiple sclerosis: assessment by the ratio of T1- and T2-weighted MR image intensity. Journal of neurology 2016;263(8):1495-1502.

47.   Laule C, Vavasour IM, Zhao Y, et al. Two-year study of cervical cord volume and myelin water in primary progressive multiple sclerosis. Multiple sclerosis (Houndmills, Basingstoke, England) 2010;16(6):670-677.

48.   Chen HS, Holmes N, Liu J, Tetzlaff W, Kozlowski P. Validating myelin water imaging with transmission electron microscopy in a rat spinal cord injury model. NeuroImage 2017;153:122-130.

49.   Harkins KD, Valentine WM, Gochberg DF, Does MD. In-vivo multi-

exponential T2, magnetization transfer and quantitative histology in a rat model of intramyelinic edema. NeuroImage Clinical 2013;2:810-817.

50. Lucchinetti CF, Guo Y, Popescu BF, Fujihara K, Itoyama Y, Misu T. The pathology of an autoimmune astrocytopathy: lessons learned from neuromyelitis optica. Brain pathology (Zurich, Switzerland) 2014;24(1):83-97.

51. Blanc F, Noblet V, Jung B, et al. White matter atrophy and cognitive dysfunctions in neuromyelitis optica. PloS one 2012;7(4):e33878.

52. Duan Y, Liu Y, Liang P, et al. White matter atrophy in brain of neuromyelitis optica: a voxel-based morphometry study. Acta radiologica (Stockholm, Sweden : 1987) 2014;55(5):589-593.

53. Liu Y, Fu Y, Schoonheim MM, et al. Structural MRI substrates of cognitive impairment in neuromyelitis optica. Neurology 2015;85(17):1491-1499.

54. Rocca MA, Agosta F, Mezzapesa DM, et al. Magnetization transfer and diffusion tensor MRI show gray matter damage in neuromyelitis optica. Neurology 2004;62(3):476-478.

55. Aboul-Enein F, Krssak M, Hoftberger R, Prayer D, Kristoferitsch W. Diffuse white matter damage is absent in neuromyelitis optica. AJNR American journal of neuroradiology 2010;31(1):76-79.

56. de Seze J, Blanc F, Kremer S, et al. Magnetic resonance spectroscopy evaluation in patients with neuromyelitis optica. Journal of neurology, neurosurgery, and psychiatry 2010;81(4):409-411.

57. Filippi M, Rocca MA, Moiola L, et al. MRI and magnetization transfer

imaging changes in the brain and cervical cord of patients with Devic's neuromyelitis optica. Neurology 1999;53(8):1705-1710.

58.   Doring TM, Lopes FC, Kubo TT, et al. Neuromyelitis optica: a diffusional kurtosis imaging study. AJNR American journal of neuroradiology 2014;35(12):2287-2292.

59.   Jeantroux J, Kremer S, Lin XZ, et al. Diffusion tensor imaging of normal-appearing white matter in neuromyelitis optica. Journal of neuroradiology Journal de neuroradiologie 2012;39(5):295-300.

60.   Kimura MC, Doring TM, Rueda FC, Tukamoto G, Gasparetto EL. In vivo assessment of white matter damage in neuromyelitis optica: a diffusion tensor and diffusion kurtosis MR imaging study. Journal of the neurological sciences 2014;345(1-2):172-175.

61.   Liu Y, Duan Y, He Y, et al. A tract-based diffusion study of cerebral white matter in neuromyelitis optica reveals widespread pathological alterations. Multiple sclerosis (Houndmills, Basingstoke, England) 2012;18(7):1013-1021.

62.   Pichiecchio A, Tavazzi E, Poloni G, et al. Advanced magnetic resonance imaging of neuromyelitis optica: a multiparametric approach. Multiple sclerosis (Houndmills, Basingstoke, England) 2012;18(6):817-824.

63.   Rueda Lopes FC, Doring T, Martins C, et al. The role of demyelination in neuromyelitis optica damage: diffusion-tensor MR imaging study. Radiology 2012;263(1):235-242.

64.   Yu C, Lin F, Li K, et al. Pathogenesis of normal-appearing white matter

damage in neuromyelitis optica: diffusion-tensor MR imaging. Radiology 2008;246(1):222-228.

65. Yu CS, Lin FC, Li KC, et al. Diffusion tensor imaging in the assessment of normal-appearing brain tissue damage in relapsing neuromyelitis optica. AJNR American journal of neuroradiology 2006;27(5):1009-1015.

66. Zhao DD, Zhou HY, Wu QZ, et al. Diffusion tensor imaging characterization of occult brain damage in relapsing neuromyelitis optica using 3.0T magnetic resonance imaging techniques. NeuroImage 2012;59(4):3173-3177.

67. Liu C, Li W, Johnson GA, Wu B. High-field (9.4 T) MRI of brain dysmyelination by quantitative mapping of magnetic susceptibility. NeuroImage 2011;56(3):930-938.

68. Wingerchuk DM, Banwell B, Bennett JL, et al. International consensus diagnostic criteria for neuromyelitis optica spectrum disorders. Neurology 2015;85(2):177-189.

69. Matthews L, Kolind S, Brazier A, et al. Imaging Surrogates of Disease Activity in Neuromyelitis Optica Allow Distinction from Multiple Sclerosis. PloS one 2015;10(9):e0137715.

70. Zhang J, Kolind SH, Laule C, MacKay AL. Comparison of myelin water fraction from multiecho T2 decay curve and steady-state methods. Magnetic resonance in medicine 2015;73(1):223-232.

71. Maas AI, Stocchetti N, Bullock R. Moderate and severe traumatic brain injury in adults. The Lancet Neurology 2008;7(8):728-741.

72.   Katz DI, Alexander MP. Traumatic brain injury. Predicting course of recovery and outcome for patients admitted to rehabilitation. Archives of neurology 1994;51(7):661-670.

73.   Ross BL, Temkin NR, Newell D, Dikmen SS. Neuropsychological outcome in relation to head injury severity. Contributions of coma length and focal abnormalities. American journal of physical medicine & rehabilitation 1994;73(5):341-347.

74.   Kraus MF, Susmaras T, Caughlin BP, Walker CJ, Sweeney JA, Little DM. White matter integrity and cognition in chronic traumatic brain injury: a diffusion tensor imaging study. Brain : a journal of neurology 2007;130(Pt 10):2508-2519.

75.   Newcombe VF, Williams GB, Nortje J, et al. Analysis of acute traumatic axonal injury using diffusion tensor imaging. British journal of neurosurgery 2007;21(4):340-348.

76.   Shenton ME, Hamoda HM, Schneiderman JS, et al. A review of magnetic resonance imaging and diffusion tensor imaging findings in mild traumatic brain injury. Brain imaging and behavior 2012;6(2):137-192.

77.   Jurick SM, Bangen KJ, Evangelista ND, Sanderson-Cimino M, Delano-Wood L, Jak AJ. Advanced neuroimaging to quantify myelin in vivo: Application to mild TBI. Brain injury 2016;30(12):1452-1457.

78.   Mierzwa AJ, Marion CM, Sullivan GM, McDaniel DP, Armstrong RC. Components of myelin damage and repair in the progression of white matter pathology after mild traumatic brain injury. Journal of

neuropathology and experimental neurology 2015;74(3):218-232.

79. Bramlett HM, Dietrich WD. Quantitative structural changes in white and gray matter 1 year following traumatic brain injury in rats. Acta neuropathologica 2002;103(6):607-614.

80. Ng HK, Mahaliyana RD, Poon WS. The pathological spectrum of diffuse axonal injury in blunt head trauma: assessment with axon and myelin strains. Clinical neurology and neurosurgery 1994;96(1):24-31.

81. Kinnunen KM, Greenwood R, Powell JH, et al. White matter damage and cognitive impairment after traumatic brain injury. Brain : a journal of neurology 2011;134(Pt 2):449-463.

82. Sharp DJ, Beckmann CF, Greenwood R, et al. Default mode network functional and structural connectivity after traumatic brain injury. Brain : a journal of neurology 2011;134(Pt 8):2233-2247.

83. Wright AD, Jarrett M, Vavasour I, et al. Myelin Water Fraction Is Transiently Reduced after a Single Mild Traumatic Brain Injury--A Prospective Cohort Study in Collegiate Hockey Players. PloS one 2016;11(2):e0150215.

84. Avants B, Gee JC. Geodesic estimation for large deformation anatomical shape averaging and interpolation. NeuroImage 2004;23 Suppl 1:S139-150.

85. Avants BB, Yushkevich P, Pluta J, et al. The optimal template effect in hippocampus studies of diseased populations. NeuroImage 2010;49(3):2457-2466.

86. Smith SM. Fast robust automated brain extraction. Human brain mapping

2002;17(3):143-155.

87. Smith SM, Jenkinson M, Johansen-Berg H, et al. Tract-based spatial statistics: voxelwise analysis of multi-subject diffusion data. NeuroImage 2006;31(4):1487-1505.

88. Jackson WT, Novack TA, Dowler RN. Effective serial measurement of cognitive orientation in rehabilitation: the Orientation Log. Archives of physical medicine and rehabilitation 1998;79(6):718-720.

89. Mathias JL, Wheaton P. Changes in attention and information-processing speed following severe traumatic brain injury: a meta-analytic review. Neuropsychology 2007;21(2):212-223.

90. Felmingham KL, Baguley IJ, Green AM. Effects of diffuse axonal injury on speed of information processing following severe traumatic brain injury. Neuropsychology 2004;18(3):564-571.

91. Wechasler D, Coalson D, S. R. WAIS-IV: Wechsler adult intelligence scale. San Antonio, TX: Pearson: 2008.

92. Winkler AM, Ridgway GR, Webster MA, Smith SM, Nichols TE. Permutation inference for the general linear model. NeuroImage 2014;92:381-397.

93. Landman BA, Wan H, Bogovic JA, Bazin PL, Prince JL. Resolution of Crossing Fibers with Constrained Compressed Sensing using Traditional Diffusion Tensor MRI. Proceedings of SPIE--the International Society for Optical Engineering 2010;7623:76231h.

94. Maxwell WL. Damage to myelin and oligodendrocytes: a role in chronic

outcomes following traumatic brain injury? Brain sciences 2013;3(3):1374-1394.

95.   Kennedy JE, Clement PF, Curtiss G. WAIS-III processing speed index scores after TBI: the influence of working memory, psychomotor speed and perceptual processing. The Clinical neuropsychologist 2003;17(3):303-307.

96.   Chevalier N, Kurth S, Doucette MR, et al. Myelination Is Associated with Processing Speed in Early Childhood: Preliminary Insights. PloS one 2015;10(10):e0139897.

97.   Waxman SG. Determinants of conduction velocity in myelinated nerve fibers. Muscle & nerve 1980;3(2):141-150.

98.   Beaulieu C. The basis of anisotropic water diffusion in the nervous system - a technical review. NMR in biomedicine 2002;15(7-8):435-455.

99.   Wozniak JR, Krach L, Ward E, et al. Neurocognitive and neuroimaging correlates of pediatric traumatic brain injury: a diffusion tensor imaging (DTI) study. Archives of clinical neuropsychology : the official journal of the National Academy of Neuropsychologists 2007;22(5):555-568.

100.   Wang X, Cusick MF, Wang Y, et al. Diffusion basis spectrum imaging detects and distinguishes coexisting subclinical inflammation, demyelination and axonal injury in experimental autoimmune encephalomyelitis mice. NMR in biomedicine 2014;27(7):843-852.

101.   Chiang CW, Wang Y, Sun P, et al. Quantifying white matter tract diffusion parameters in the presence of increased extra-fiber cellularity and

vasogenic edema. NeuroImage 2014;101:310-319.

102. Lee HM, Kim D, Oh SS, Choi JY, Oh SH, Lee J. The phase and magnetization transfer characteristics of a novel myelin water imaging method (ViSTa). Proc Intl Soc Mag Reson Med 23rd. Volume #338; 2014.

103. Oh SH, Choi JY, Im Y, Prasloski T, Lee J. Myelin water fraction of the whole brain: 3D grase MWI vs 3D ViSTa MWI. Proc Intl Soc Mag Reson Med 23rd. Volume #3143; 2014.

Abstract

Myelin Water Imaging
for Clinical Research

Joon Yul Choi

Electrical and Computer Engineering

The Graduate School

Seoul National University

Myelin plays an important role in transmitting electrical signals in the body. Neurodegenerative diseases are associated with myelin damage and induce a loss of the electrical signals. The conventional T_1 and T_2 weighted imaging, used in clinics, cannot quantify the amount of myelin and confirm the degree of myelin damage in patients with neurodegenerative diseases. This thesis applied newly developed myelin water imaging, named ViSTa, to the neurodegenerative diseases to estimate changes in myelin. To utilize ViSTa myelin water imaging in clinical studies, I explored the effects of water exchange and inflow in ViSTa myelin water imaging. Then, I developed new data analysis pipelines to apply ViSTa myelin water imaging for the clinical studies. First, the Monte-Carlo simulation model that has the biological and physical properties of white matter fiber was developed for myelin water residence time. The simulation model validated the origin of ViSTa as myelin water. Second, the thesis developed a flow simulation model to compensate artifacts from inflow blood in ViSTa myelin water imaging. The flow simulation

model suggested the optimal timing of flow saturation pulse(s) to suppress the inflow of blood. Finally, I summarized new data analysis pipelines for clinical applications. Using the analysis pipelines, ViSTa myelin water imaging revealed reduced apparent myelin water fraction in normal-appearing white matter for three prominent brain diseases and injury (neurodegenerative diseases): multiple sclerosis, neuromyelitis optica spectrum disorders, and traumatic brain injury. The developments in this thesis can be utilized not only in the diagnosis, treatment, and prognosis of various diseases but also in neuroplasticity and rehabilitation studies to explore the answer for the questions related to myelin issues.